Development and Flight Test of Moving-mass Actuated Unmanned Aerial Vehicle

by

SAMPATH REDDY VENGATE

Presented to the Faculty of the Graduate School of
The University of Texas at Arlington in Partial Fulfillment
of the Requirements
for the Degree of

MASTERS IN AEROSPACE ENGINEERING

THE UNIVERSITY OF TEXAS AT ARLINGTON
May 2016

Dedicated to my family and friends

ACKNOWLEDGEMENTS

First, I would like to thank my supervising professor Dr.Atilla Dogan for his continuous guidance and support over the years of my research at The University of Texas Arlington. During this tenure under Dr.Dogan I learnt a lot on problem solving techniques, he was always their to help and encourage me throughout my thesis work. He believed in me and put in high amount of investment in terms equipment, provided facilities and more importantly his knowledge. I could not have imagined a better guide and advisor for my masters thesis. I am really grateful to Dr.Dogan for providing me an opportunity to work under him.

I convey my regards to Dr.Huff, Dr.Smith and Dr.Subbarao for taking time to be on my thesis committee. I am grateful to Dr.Huff for having me on the SUAS Team, which kept me going with my Flying in these two years.

Beside this, I would like to thank Onur for supporting me throughout. I also want to thank all my friends who helped me during my test flights and it would have been really difficult for me to carry-out the tests alone.

Lastly, I am greatful to my parents,teachers, friends for their everlasting support and inspiration, with out them it would have been impossible for me to complete this assignment.

May 3, 2016

ABSTRACT

Development and Flight Test of Moving-mass Actuated Unmanned Aerial Vehicle

Sampath Reddy Vengate, M.S.

The University of Texas at Arlington, 2016

Supervising Professors: Dr. Atilla Dogan

Conventional airplane control is achieved by aerodynamic control surfaces by generating moments around all the three axes of the aircraft. Deflections of the control surfaces have some disadvantages such as induced drag, increase in radar signature, and exposure to high temperature in high speed applications. As an alternative moment generation mechanism, prior research proposed internal mass-actuation, which is to generate gravitational moment by changing the center of gravity of the aircraft through motion of internal masses within the aircraft. Prior research investigated the feasibility and benefit of internal mass-actuation in airplane control based on simulation analysis. The main focus of this research is to design, build and flight test a UAV (Unmanned Aerial Vehicle) with internal mass-actuation, as a proof-of-concept. Specifically, this effort has built and flight tested a small electric powered UAV with an internal mass within each wing to generate rolling moment instead of aerodynamic rolling moment by ailerons. The internal structure of each wing is specifically designed to place a linear electric actuator that moves the internal mass. The aircraft is also equipped with all three conventional control surfaces. Most parts of the airplane were laser cut based on 3D CAD designs. The airplane is also equipped with a data acquisition system to record flight data during the flight test. The RC (radio control) transmitter is programmed to switch between aileron-actuation and mass-actuation. During test flights, an RC operator flew the airplane to a steady level flight at a safe altitude, and then switch to mass-actuation and put the airplane in steady-turn. The flight tests has successfully demonstrated the feasibility of flying the airplane with mass-actuation instead of ailerons.

TABLE OF CONTENTS

LIST OF FIGURES

Figure Page

CHAPTER 1

Introduction

This chapter explains the problem statement for the thesis research work. It also presents some literature review, the motivation for carrying out this research and finally gives a brief description on thesis organization.

1.1 Research Motivation

Aircraft generate aerodynamic moments using control surfaces. The control surfaces deflect the flowing air over them, thus creating the particular roll, pitch or yawing moments. There are some drawbacks in using control surfaces for generating aerodynamic moments, which are stated as follows:

1. Drag created during deflection: Every time a control surface deflects, deflecting the air over it creates a certain amount of drag and lift loss. In order to overcome this drag, the aircraft needs to use more amount of power.

2. Control authority depends on airflow: Aerodynamic control surfaces require airflow over them at every instant in order to generate the required moments. In case of low airspeed, there is less control authority.

3. Adverse Yaw effect: During a rolling moment generated by ailerons, an aircraft naturally tends to yaw in the opposite direction of the roll called an adverse yaw due to the difference in profile drag between the upward and downward deflected ailerons.

4. Stealth applications: Technologies of avoiding detection by radars for aircraft vary widely. Deflection of control surfaces is known to increase detection rate. Thus,

eliminating control surface deflection by using internal mass actuation can be proven advantageous.

5. Hypersonic vehicle applications: Aircrafts traveling at hypersonic velocities undergo a lot of thermal and structural effects. The control surfaces deflection at these speeds causes a high disadvantage to the aircraft and its performance. Thus, mass actuation system can be a solution.

Therefore, elimination of control surfaces will help simplify wing and tail design and improve aerodynamic performance of the aircraft. This can yield power conservation leading to longer flight durations, enable low speed operations and various other advantages as discussed above with certain applications. With this motivation, we try to develop a mechanism for an Unmanned Aerial Vehicle to generate aerodynamic moments using a moving-mass actuation system which would address all the above mentioned backdrops and improve the performance of the aircraft.

1.2 Literature Review

Actuation mechanisms with moving masses has been proposed and/or used for space [1], aerial [2–5] and underwater [6,7] vehicles. Ref. [1] proposed repositioning small masses within spacecraft for formation control in order to achieve orbit control without mass expulsion. Ref. [2] suggested a moving-mass trim controller for maneuvering an axi-symmetric re-entry vehicle. Three independently located equal masses are used to achieve the required change in the center of mass location. Attitude control of a spinning vehicle is investigated using internal moving-mass trim controller in [3]. Ref. [4] showed that moving-mass actuation maintains constant control effectiveness and generates high enough amount of moments for maneuvering and attitude control of a re-entry vehicle. Ref. [5] used moving-mass actuators for kinetic warheads and addressed the issue of having sufficient internal space to accommodate moving-mass actuators without effecting the static stability characteristic. In addition to space and re-entry vehicles, underwater vehicles have also employed internal mass actuation for increasing cruise speed, improving depth control and maintaining maneuverability in various operating conditions [6]. Ref. [7] illustrated that moving-mass actuation allows low speed operations and is not susceptible to corrosion or biological contamination. Refs. [8],[9],[10],[11] and [12] demonstrate the feasibility of implementing moving mass actuation systems inside an Unmanned Aerial Vehicle (UAV) by performing various trim analysis in steady turn, in turns with zero side slip and controllability analysis.

1.3 Thesis Objective

This research is to do a proof-of-concept study to demonstrate the feasibility of mass actuation in a small Unmanned Aerial Vehicle (UAV). The motivation is to eliminate drag increase and lift loss caused by deflection of control surfaces by replacing them with internal moving-mass actuators as alternative moment generation mechanisms. Substitution of control surfaces with moving masses may also help simplify wing and tail design and enhance the aerodynamic performance of the aircraft. To determine whether the use of moving-mass actuation should be seriously considered, a mechanism should be developed in order to perform a set of experiments to analyze the feasibility and limits of the concept proposed.

This thesis presents the first step towards implementing the moving mass actuation system on an Unmanned Aerial Vehicle. This thesis focuses on design, built and flight test analysis of a mass actuated aircraft. A UAV is developed with two moving-mass actuation units installed on either side of the wing for rolling moment generation. Aircraft dynamics model is chosen from an earlier theoretical study performed on moving mass actuation in a UAV [11], which consists of a mass moving in both longitudinal and lateral axis. This dynamics model is modified to simulate the two sets of actuator mechanisms, which will be discussed in a following sections. The actuation system employed in this work has certain limitations (i.e., the amount of stroke length it can operate within the wing). An analysis is performed to determine the maximum rolling moment generated within the actuator operation limit. These operations are conducted at a constant altitude and speed for both left and right, banking motion and steady turn.

1.4 Thesis Organization and Contribution

1.4.1 Thesis Organization

This thesis is organized as follows. Section II describes the description of the UAV, its blueprint, design and manufacturing procedure, propulsion system, all the electronic system with their layout and the development of the actuator mechanism. Section III presents a set of equations of motion which were adopted from the studies in reference papers, simulation cases considered and their results. Section IV consists of the test flight procedure, data acquisition and analysis procedure, and flight test results. The conclusions and future work are stated in Section V.

1.4.2 Contribution

The main contribution of this research work is to enable a UAV platform to perform banking motion and steady turn using the moving mass actuation system developed. This will serve as a proof of concept, that conventional aerodynamic control surfaces can be replaced with moving mass actuation systems in order to generate aerodynamic moments in an aircraft. This mechanism will eliminate all the drawbacks of the conventional system mentioned in the research motivation and result in flights with extended range and endurance.

CHAPTER 2

Description of Unmanned Aerial Vehicle (UAV) Developed

2.1 General Description

Moving mass actuation system requires a very stable platform for flight testing. We require an aircraft with high glide and low sink rate in order to recover the aircraft in case of any malfunction in the system. The aircraft for testing has been built with the following characteristics in mind:

1. A platform like a glider with an aspect ratio of 8: Aircrafts with aspect ratio higher than 5 are less agile and much stable, which is the prime requirement of our platform.

2. A semi-symmetrical airfoil: Such airfoils create maximum amount of lift and do not require any initial angle of attack to lift off as in the case of a symmetrical airfoil. NACA-2412 airfoil is a slow speed airfoil; this is used in few trainer aircrafts like Cessna 152, 172 and 182 airplanes and is the ideal choice for this study.

3. An airfoil with thickness 12% of the chord length (0.12 chords): Since the moving mass actuation system is placed inside the wings, which requires a thick airfoil section to accommodate the Electric Linear Actuator. Also, we need an airfoil not so thick to avoid high drag. Thus, an intermediate value of .12 (c) is chosen.

4. A puller configuration for propulsion: This setup is chosen (i.e motor placed in the front) in order to have all the propeller wash over the aircraft which gives good performance and has adequate control authority.

2.2 Aircraft External Dimensions

This section discusses the external dimensions and the blue print development of the UAV. The initial and prime aspect of designing an aircraft is deciding the profile of the aircraft, i.e, if its a jet (which have high operating speed ranges) or a trainer (which have intermediate speed ranges) or glider (which have low speed ranges). Some other aspects to be considered are as follows: Wing position of the aircraft, gross takeoff weight of the aircraft, wing loading of the aircraft, aspect ratio of the aircraft, etc. This section explains how all these questions are answered.

The specifications of the aircraft geometry are discussed below:

1. Wing: The main reference geometry of an aircraft is the wing. Depending upon the span of the wing, the remaining aircraft dimensions are calculated. The Wingspan of the UAV is 1600 mm with a chord length of 200 mm, which gives an aspect ratio of 8.0, as shown in Fig. 2.1. With these proportions, the UAV falls into the glider category of aircraft.

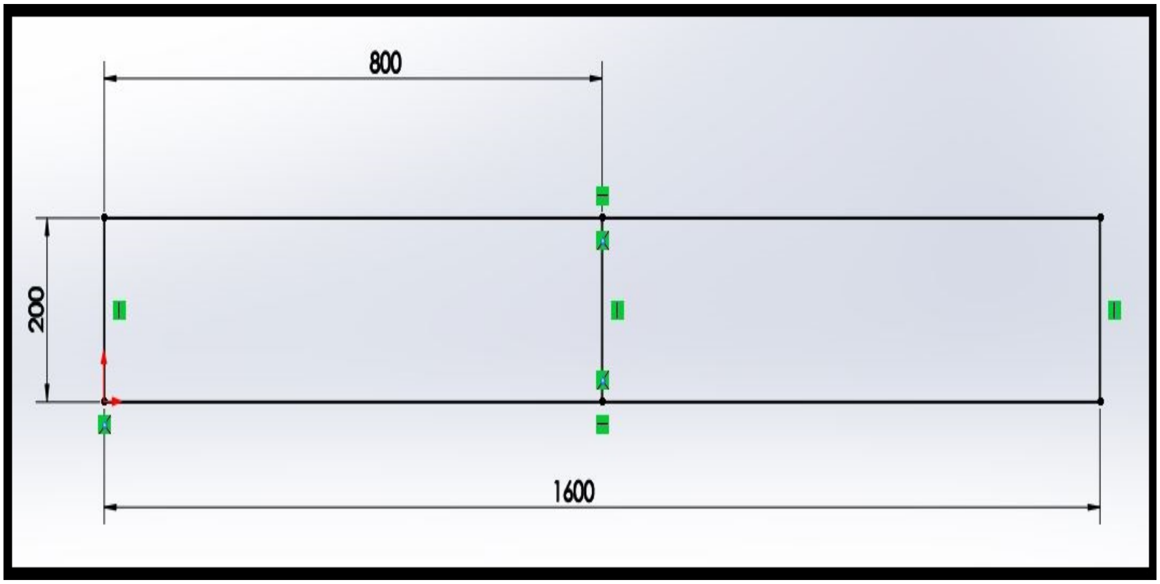

Figure 2.1. Wing dimensions.

2. Fuselage: The Fuselage is constructed with respect to the Wing dimension. The Fuselage length is ideally 3/4 th of the Wingspan which is 1200 mm in our case. The height of the fuselage is chosen according to the amount of equipment to be placed inside the aircraft keeping in mind the cost of drag creation because of thicker body size. The aircraft is of variable heights while observed from nose to tail consisting of maximum height of 100 mm at the wing mount and 50 mm at the tail. The cross-section of the aircraft also varies from nose to tail having 75 mm in the middle of the airframe and 55 mm at the tail, which is illustrated in the Fig. 2.2.

Figure 2.2. Fuselage dimensions.

3. Elevator: The Elevator of an aircraft plays a major role of horizontal stability, controls the position of the nose of the aircraft and the angle of attack of the wing. The length of the Elevator varies from 1/3 rd to 1/4 th of the wingspan. The aircraft

with elevator 1/3 rd of the wingspan has more gliding characteristics when compared to an elevator 1/4 th of the wingspan. This mainly helps the pilot during the final approach to flare and allows him to achieve a touchdown rate of descent which the undercarriage can absorb. Since the aircraft configuration chosen by us is a glider the Elevator dimension selected is 1/3 (Wingspan), which is rounded up to 540 mm and width being 150 mm (3/4 of wing chord) with variable cross-section Fig. 2.3.

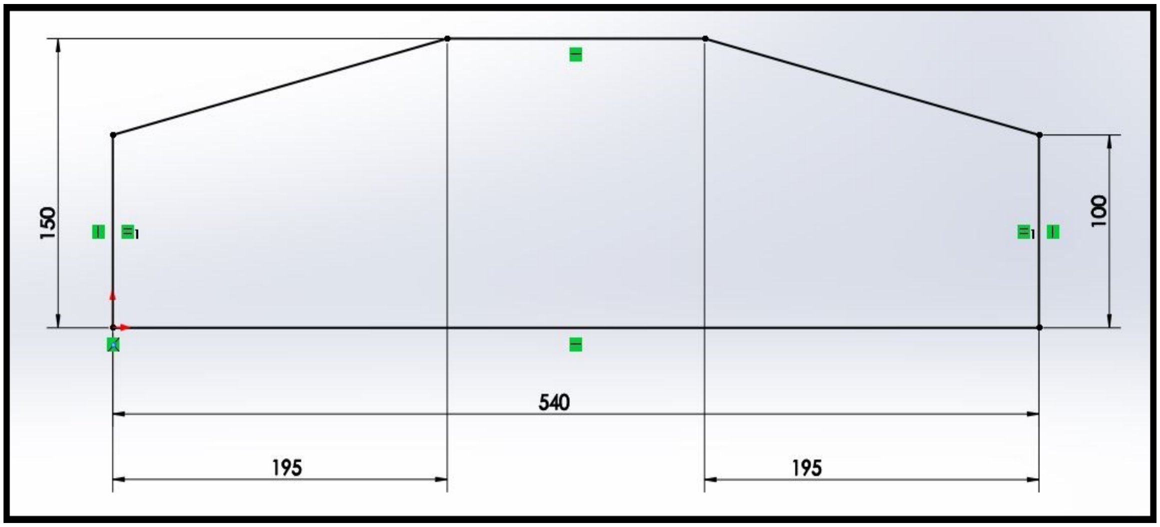

Figure 2.3. Elevator dimensions.

4. Rudder: The Rudder of an aircraft is responsible for the vertical stability of an aircraft which prevents side-to-side, or yawing, motion of the aircraft nose. The length of the rudder is with respect to the elevator, i.e, 1/2 of the elevator span or 1/6 th - 1/8 th of the wingspan. The UAV built is also equipped with a Dorsal fin. Its main purpose is to improve directional stability in high side-slip situations (asymmetric flight due to engine failure, crosswind landings, etc). The double-sweep of the leading edge of the vertical stabilizer helps the vertical stabilizer to be effective at a larger range of side-slip angles (high lateral angles of attack) Fig. 2.4.

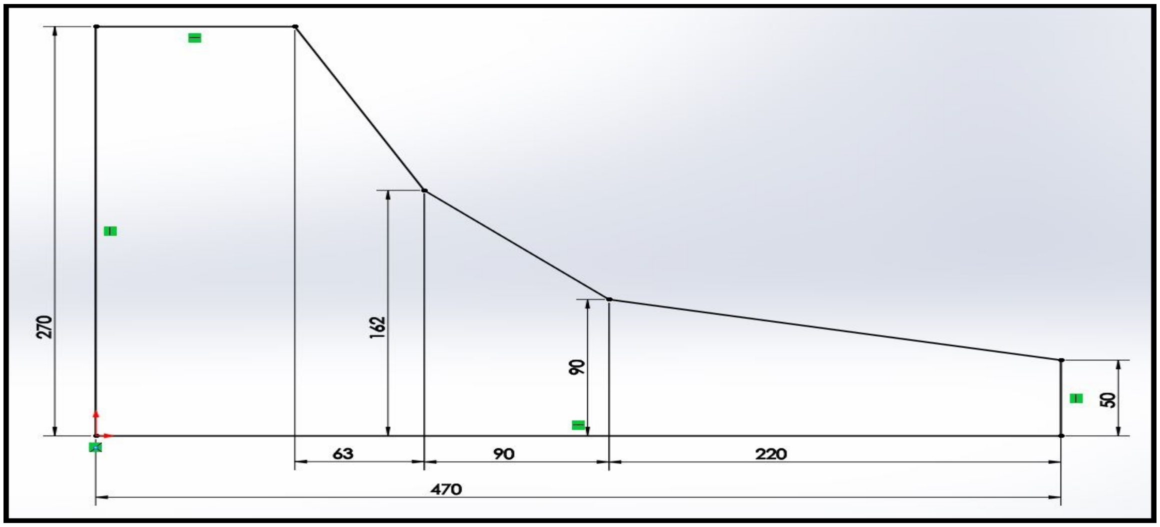

Figure 2.4. Rudder dimensions.

5. Wing Mounting position: The aircraft wing is mounted at a distance of 1/4 th of the length of the fuselage measured from the nose. The leading edge of the wing is placed at distance of 300 mm from the nose (which is 1/4 th fuselage length from its nose). Fig. 2.5 shows the positioning of the wing on the fuselage.

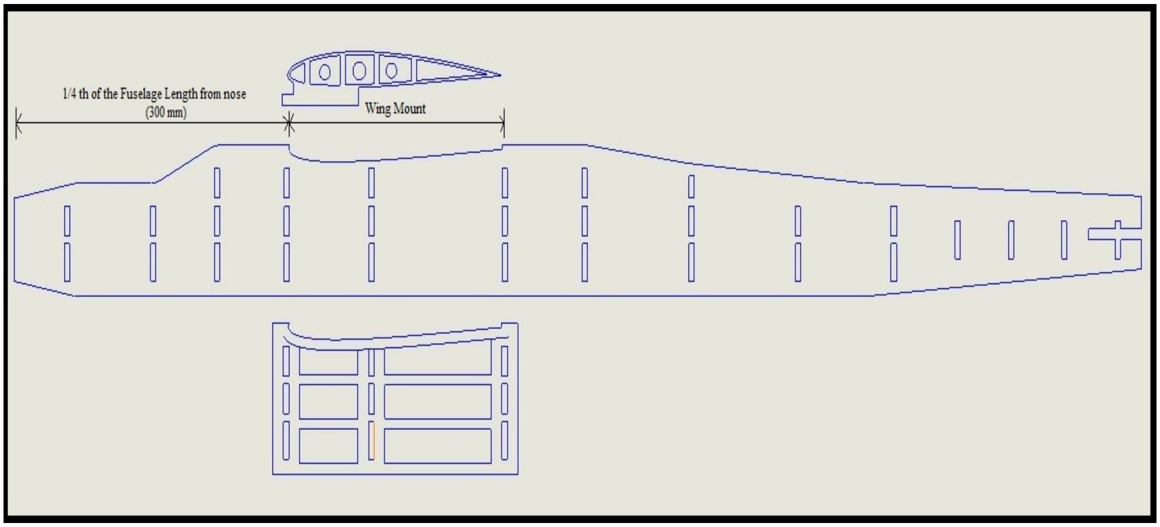

Figure 2.5. Wing mount position.

6. Dihedral Angle: Since the aircraft is being tested for the lateral moment generation using moving-mass actuation system, we have considered a flat wing configuration without any dihedral. Since dihedral angle produces a natural lateral stabilizing effect, it is a disadvantage for the study performed.

7. Airfoil Nomenclature: This section deals with one of the most important factor of an aircraft's flight performance, i.e, the airfoil section. Fig. 2.6 shows the schematic representation of the airfoil section considered for the aircraft. It is a semi-symmetrical airfoil (NACA-2412) with a thickness of 0.12c. Four-digit series airfoils by default have maximum thickness at 30% of the chord (0.3 chords) from the leading edge. Airfoils with thickness approximately 10-12 percent of their wing chord create less drag which is the requirement of our purpose.

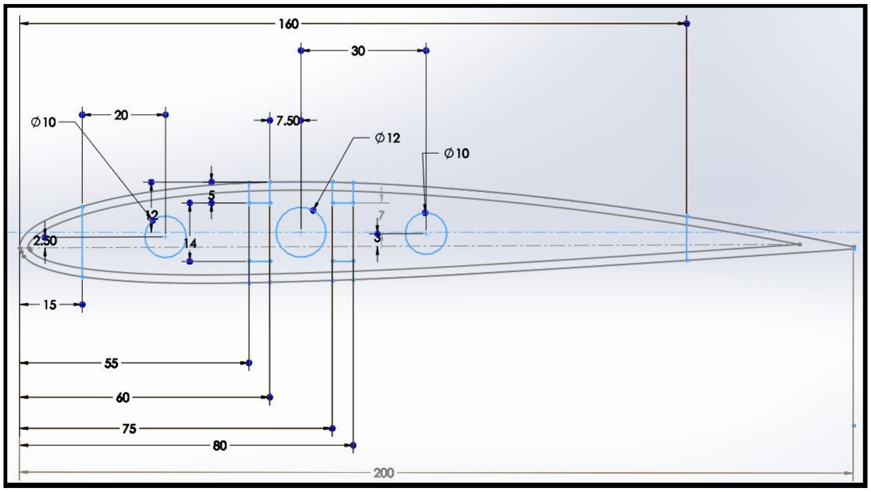

Figure 2.6. Airfoil Dimensions.

As shown in Fig. 2.6, the airfoil consists of 3 circular pockets for the wing spars. The slots towards the leading and trailing edge of the airfoil are of 10mm diameter and the center slot is of 12mm diameter. Since there will be a significant amount of hollow part in the center of the wing in order to accommodate the mass

Table 2.1. Airfoil Parameters (mm)

Parameter	Reading
$ChordLength$	200
$Thickness$	24
$LeadingEdgeRadius$	12.5
$ControlSurfaceLength$	40
$SparLocation$	35, 67.5, 100.5

actuation system, the wing may loose its strength. The leading and trailing edge spars compensate the strength loss due to the central actuator section. For having adequate control authority and sensitivity, the aerodynamic control surfaces are chosen to be 20 percent of the wing chord (i.e 40mm).

Table 2.2. Basic Dimensions of the Aircraft (mm)

Parameter	Reading
$WingSpan$	1600
$AspectRatio$	8
$FuselageLength$	1200
$ElevatorLength$	540
$ElevatorWidth$	150
$RudderLength$	270

Table. 2.2 consists of all the aircraft basic dimensions. All the dimensions mentioned above are in metric. The following section discusses in detail the design of the aircraft structural components, their fabrication and assembly.

2.3 Design, Manufacturing and Assembly of the Structure

With the help of calculated dimensions of the aircraft during the initial phase of blueprint development, the design and manufacturing is performed. This section describes the design of the internal structural components, followed by the building process. Initially, the bulkheads of the fuselage, fuselage panel and airfoil sections of the wing were designed in SolidWorks. Later these templates were cut using a carbon-dioxide laser cutter. The laser uses various speed and laser intensity specifications for each material. These specifications also vary for etching and through cutting. All the bulkhead and airfoil templates are cut through and their respective numbers are etched on them. A speed of 1000 with 0.85 laser intensity was used for cutting and 1500 speed with 0.10 laser intensity was used for etching the labels on balsa wood.

The images in Fig. 2.7 shows the complete set of structural components of the aircraft designed in 2-D in SolidWorks.

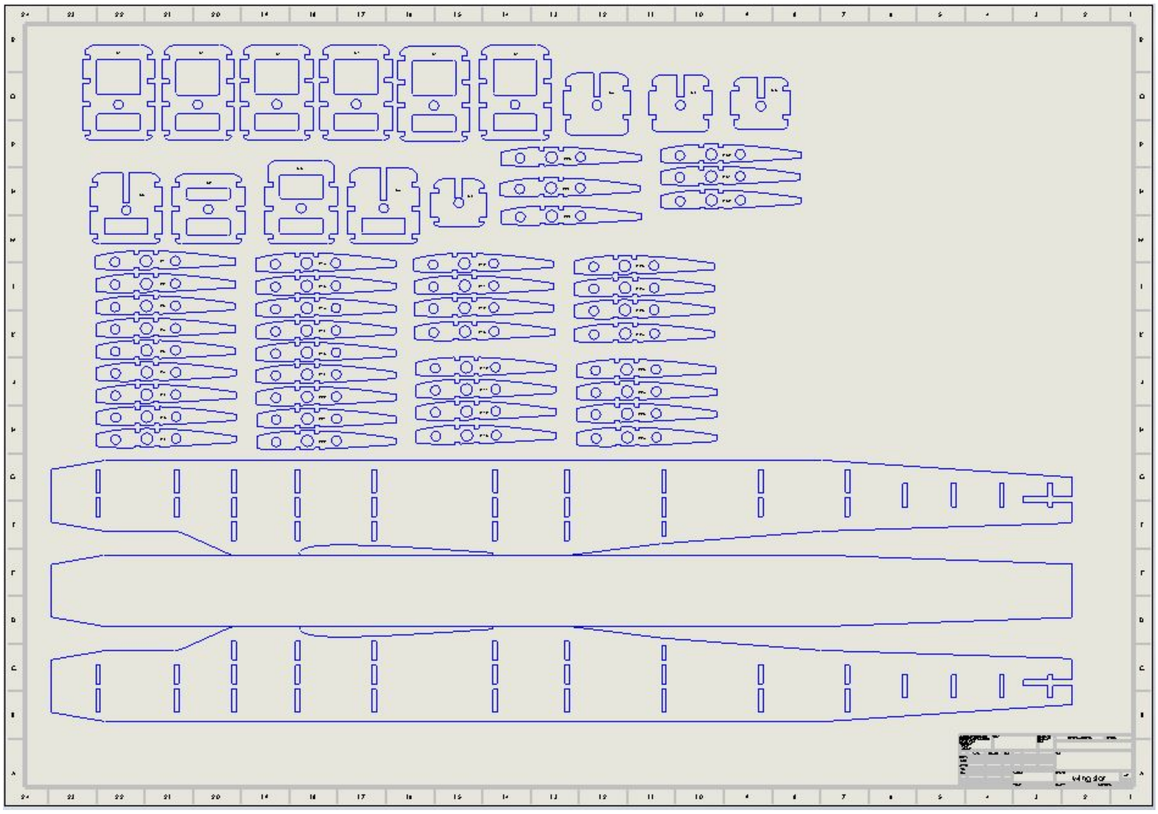

Figure 2.7. Bulkheads, Fuselage Panel and Airfoil Section Designs .

Figure 2.8. Laser cut cardboard templates.

Before cutting the balsa templates, a set of cardboard templates where cut and dry fitted to check for alignment and design accuracy. Fig. 2.8 shows the laser cut templates with cardboard assembly.

After fine refinement of the designs, balsa templates are cut (see Fig. 2.9). These sections were assembled together for completing the airframe. As observed in the images, the bulkheads consist of circular pockets which were designed for their alignment during assembly. These were flushed with the fuselage panels on either sides of the walls with a base plate at the bottom. The aircraft nose is carved down into a conical form in order to allow the propellers to fold to the contour when set to idle and land without hindrance as shown in Fig. 2.10. Later the empennage of the aircraft is constructed by hand-cutting. The internal structure of the elevator and rudder are shown in Fig. 2.11.

Figure 2.9. Laser cut balsa templates of whole aircraft.

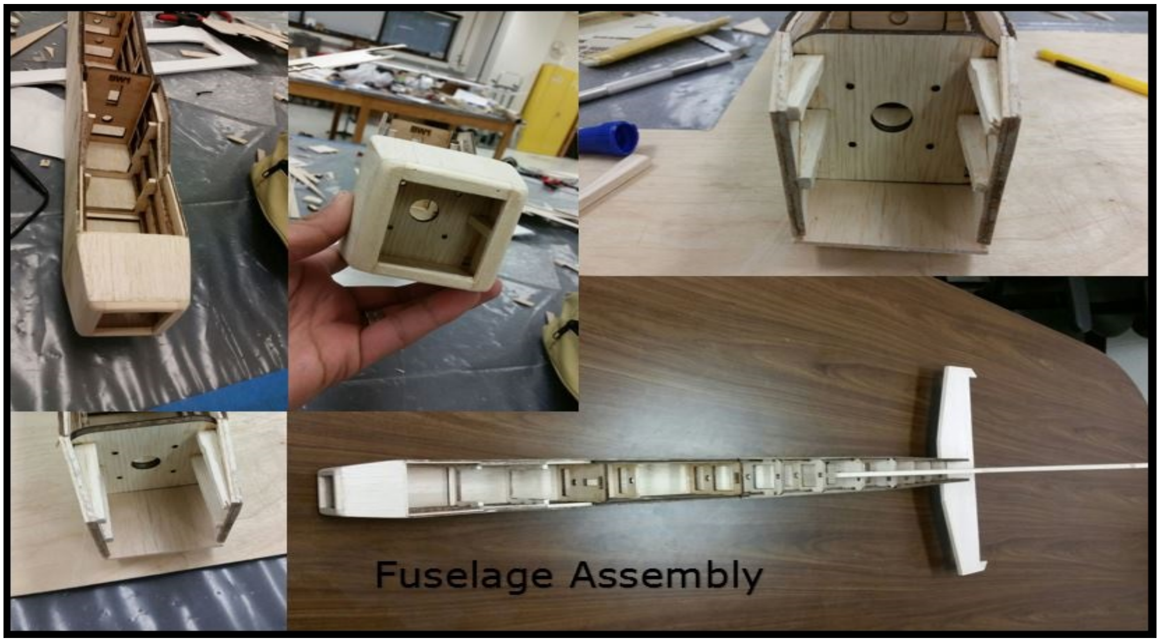

Figure 2.10. Fuselage assembly with empennage.

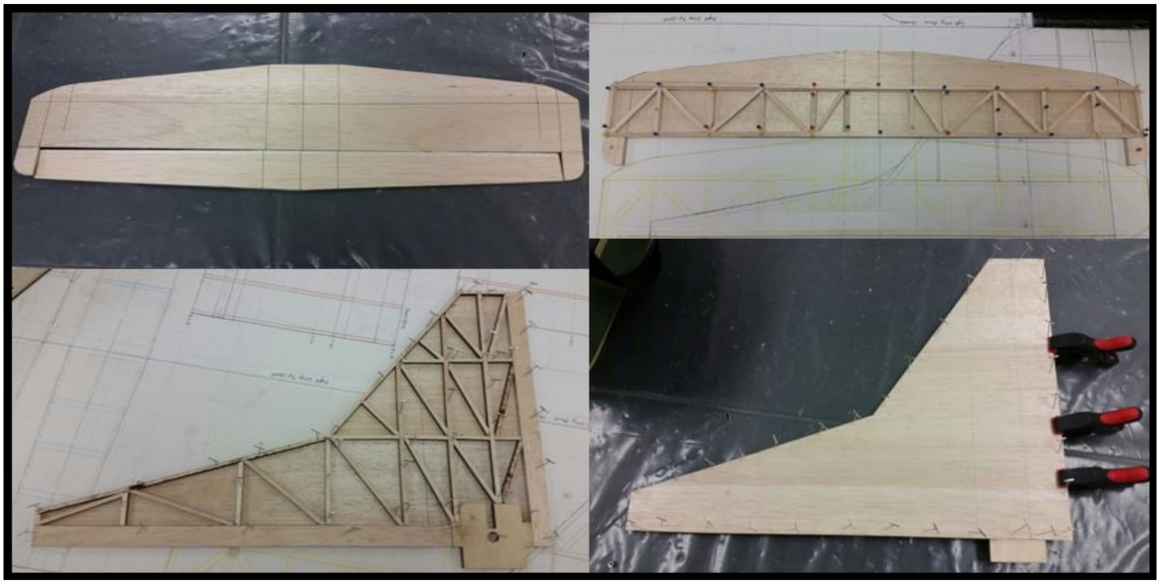

Figure 2.11. Empennage Construction.

In the most crucial section of the aircraft assembly (Wings), wings are assembled with the help of the spars which set a base for the wing rib alignment. The aircraft is equipped with 3 spars as shown in Fig. 2.12. Since the aircraft wing will accommodate the linear actuators in the central part of the wings, an additional spar towards the leading and trailing edge of the wing is required to maintain the required amount of strength. The linear actuators will be placed in a compartment in the center of the wing at a distance of 350mm from the center of the wing on either side. These are designed as line replaceable units (LRU's) in order to remove/replace at any given time.

The aircraft is provided with two canopies for accessing the electronic components both in the nose and tail part as shown in Fig. 2.13. The aileron and flap actuators are also fitted into cabinets inside the wing for easy access and modifications. Figs. 2.12 and 2.14 showcase the complete build process of the wing representing the essential features of the aircraft described above.

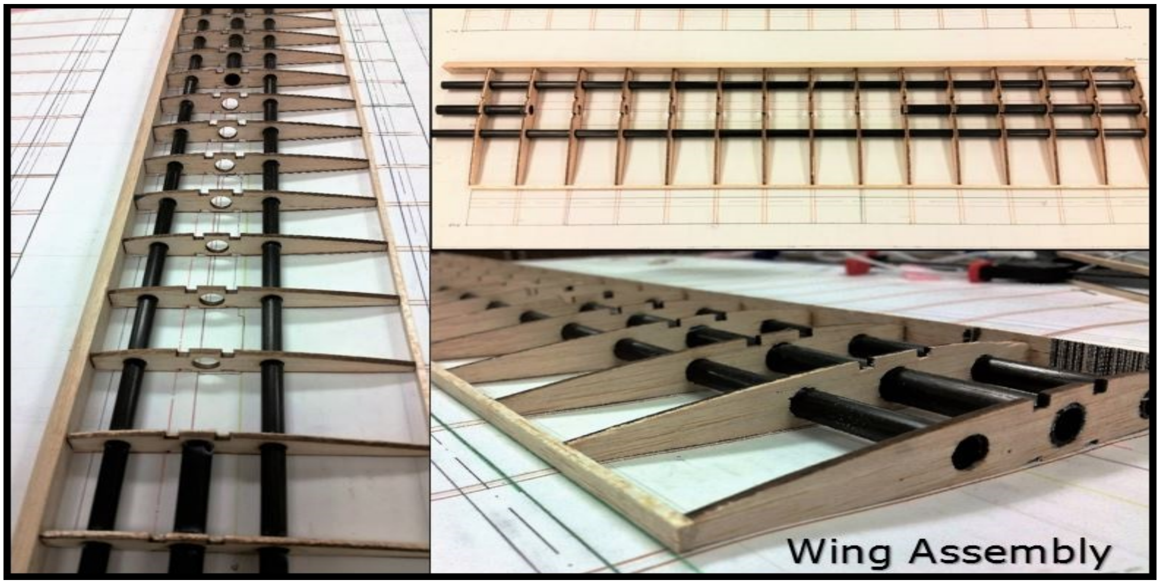

Figure 2.12. Wing Assembly.

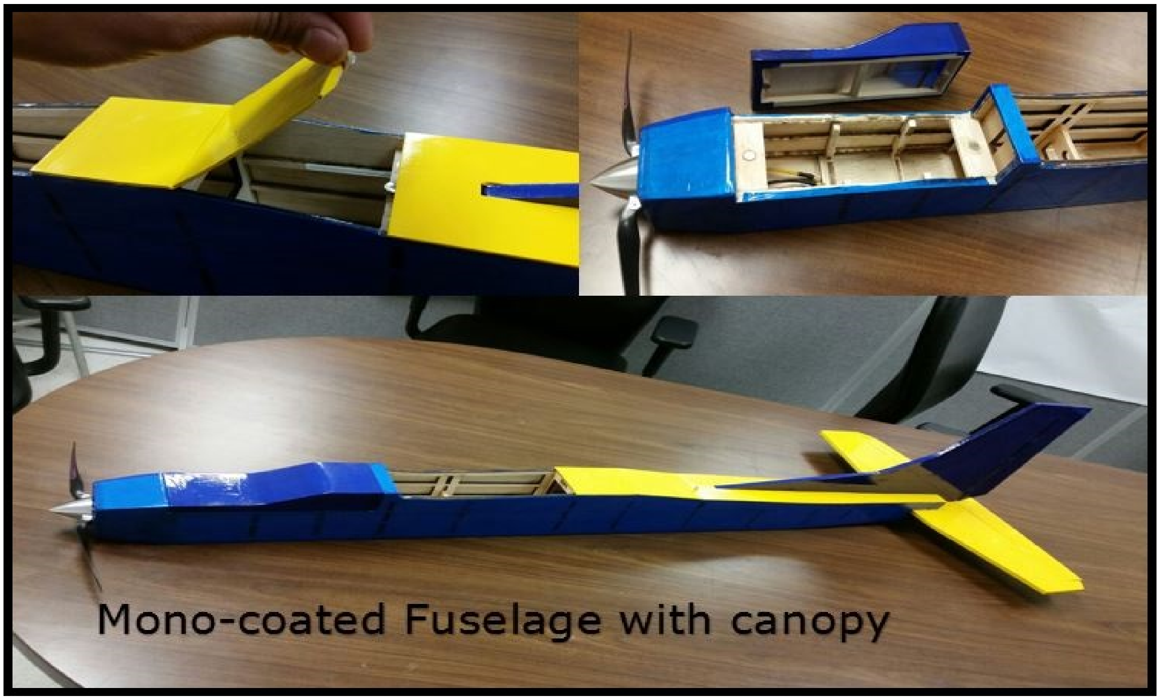

Figure 2.13. Complete Fuselage Frame.

Figure 2.14. Linear Actuator slots with Electronics.

The wing sheeting consists of certain slots in order to reduce the weight of the aircraft. These slots will be covered by the mono-coat sheeting and will have the same contour as a fully covered wing. We can also observe in Fig. 2.15 that the wing tips are designed with a sweep angle. These are to reduce the wing-tip vortices during the flight. Also, the ailerons and flaps are of equal sizing on either side of the wing.

The wings are bolt mounted on to the aircraft fuselage. For this mounting system, a specific locking method is used. The airfoil ribs of both the wings towards the root of the wing joint are equipped with a extra wooden hinge in their leading edge. This hinge is locked on to the front part of the fuselage mount and the trailing edge of the wing is locked with a set of two nylon bolts threaded on to a blind nut mount inside the aircraft as shown in Figs. 2.16 and 2.17.

Figure 2.15. Wing Sheeting.

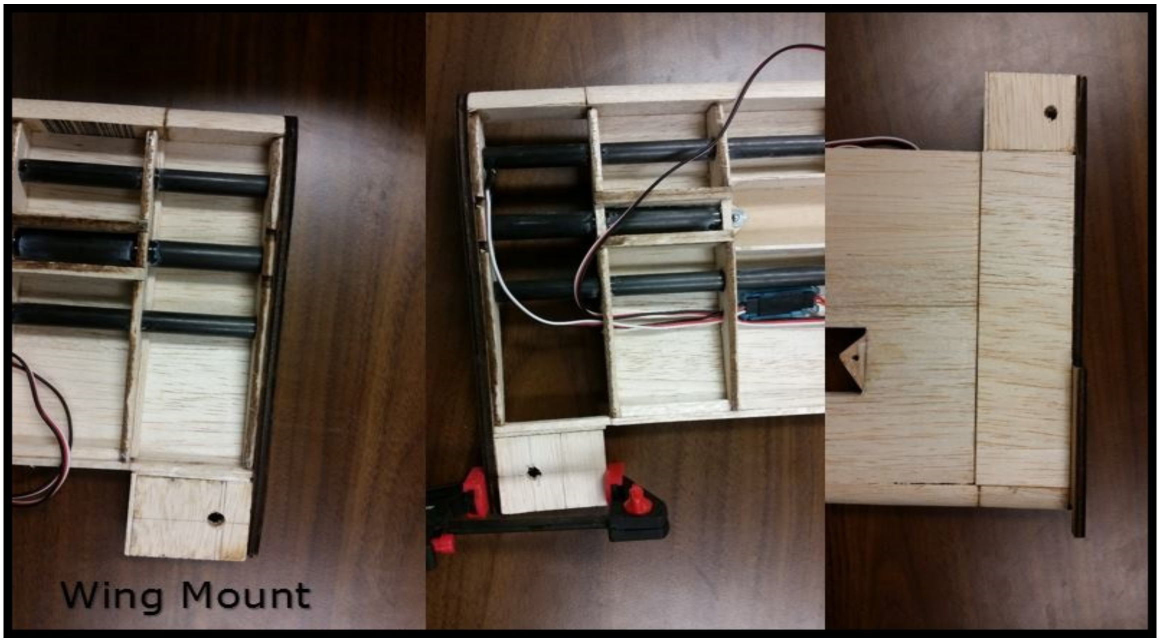

Figure 2.16. Wing Mount Design.

A completely assembled aircraft with mono coating and electronics installation is shown in Fig. 2.17.

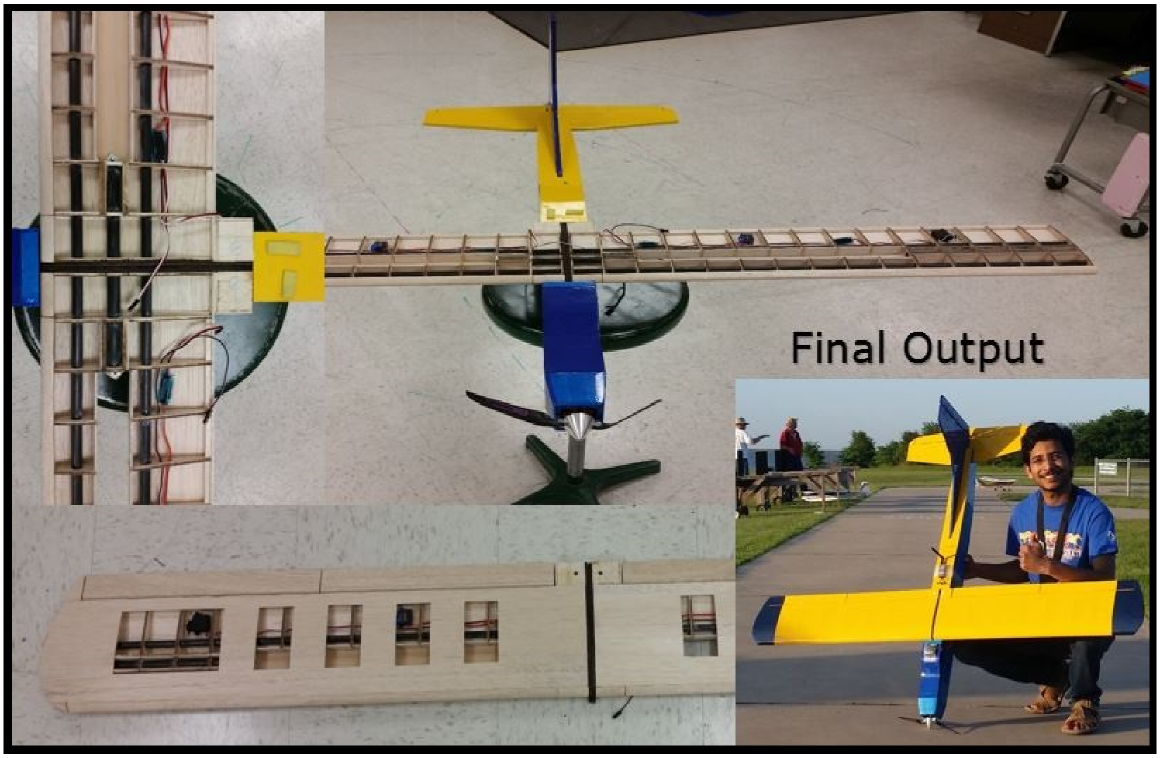

Figure 2.17. Final Assembly.

2.4 Propulsion System

The total takeoff weight of the aircraft is 3.0 kgs. This creates a requirement of a propulsion system which could generate adequate amount of thrust for propelling the aircraft. Turnigy D3548/4 1100KV Brushless motor [13] is chosen for this configuration, which produces about 3.6 kgs of thrust with a 60 amp electronic speed controller (ESC) [14] in combination with a 11x8 propeller and 14.8V 4S Lithium Polymer battery [15]. The aircraft is equipped with a folding propeller in order to eliminate the landing gear to reduce the total takeoff weight. Tables. 2.3, 2.4, and 2.5 give the specifications of the power unit described.

Table 2.3. Turnigy D3548/4 1100KV Brushless Outrunner Motor

Parameter	Reading
$CountinuousCurrent$	50-55 A
$MaximumBurstCurrent$	60 A
Kv	1100 rpm/V
$Voltage, Vm$	7.4 14.8 V
$Power, W$	910 W
$Mass, Mm$	159gms
$MaximumThrust, Kg$	3650gms

Table 2.4. Turnigy 5000mAh 4S 25C Lipo Pack

Parameter	Reading
$Capacity, Cb$	5000mah
$Voltage, Vm$	14.8 V
$MaximumConinuousDischarge$	40 C
$PeakDischarge$	45 C (10sec)
$Mass, Mb$	548gms

Table 2.5. Turnigy Plush 60 amp ESC

Parameter	Reading
$ConstantCapacity, A$	60amps
$InputVoltage, Vm$	5.6 - 22 V
$BurstCurrent$	80 amps
BEC	5V/3A
$Mass, Mb$	60gms

Figure 2.18. Propulsion System of the aircraft.

2.5 Actuators for Aerodynamic Control Surfaces

The aerodynamic control surfaces are equipped with two different servo systems. The elevator and rudder consists of HITEC 85MG digital metal gear servos [16], whereas the ailerons are equipped with ADAFRUIT Feedback Micro Metal gear servos [17]. These servos are configured such that they produce a deflection of -/+ 80 degrees on their control surfaces for having high sensitivity. Tables 2.6 and 2.7 give the specifications of these servos.

Table 2.6. HITEC 85MG Digital Metal gear servo

Parameter	Reading
$Torque, T$	3.0 kg-cm @ 6V
$Speed$	0.16 sec/60 degrees @ 6V
$Mass, Mb$	21 gms

Table 2.7. ADAFRUIT Feedback Micro Metal gear servo

Parameter	Reading
$Torque, T$	1.8 kg-cm @ 6V
$Speed$	0.1 sec/60 degrees @ 6V
$Mass, Mb$	15.8 gms

These servos on aileron are equipped with a feedback line from its potentiometer to provide the position information of the aileron deflections. All these servos are input into an autopilot kit, called Pixhawk and will be discussed in detail in Section 2.7.

2.6 Actuators for Moving-Masses

The mechanism for the moving-mass system consists of two Linear Electric Actuators placed inside either of the wings with a Control Board. The actuators chosen are Firgelli L-16 P-Series [18]. It has an axial design that utilizes a powerful PMDC motor and a rectangular cross section for increased strength. The P-Series actuator has an internal linear potentiometer that provides position feedback, which can be input to an external controller. The P-Series can be used with the Linear Actuator Control Board (LAC) to give the P-series the ability to be controlled with

USB (via our Configuration Utility Software), 0-5v, 4-20mA, RC Servo or PWM. Onboard adjustment of speed, sensitivity and stroke limits are available via the LAC. Fig. 2.19 shows the data sheet of the linear actuator.

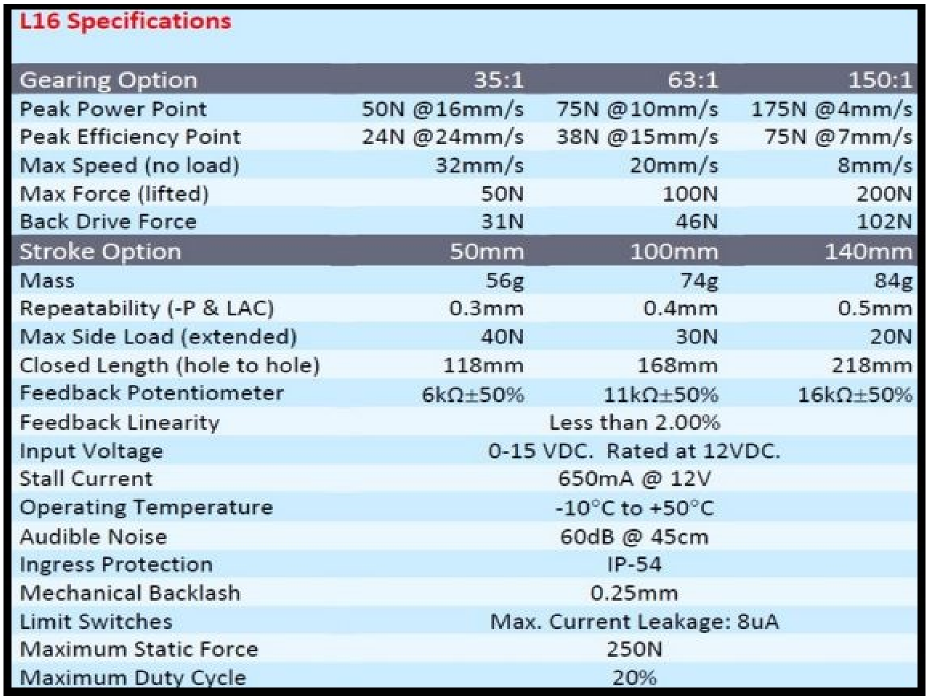

L16 Specifications

Gearing Option	35:1	63:1	150:1
Peak Power Point	50N @16mm/s	75N @10mm/s	175N @4mm/s
Peak Efficiency Point	24N @24mm/s	38N @15mm/s	75N @7mm/s
Max Speed (no load)	32mm/s	20mm/s	8mm/s
Max Force (lifted)	50N	100N	200N
Back Drive Force	31N	46N	102N
Stroke Option	**50mm**	**100mm**	**140mm**
Mass	56g	74g	84g
Repeatability (-P & LAC)	0.3mm	0.4mm	0.5mm
Max Side Load (extended)	40N	30N	20N
Closed Length (hole to hole)	118mm	168mm	218mm
Feedback Potentiometer	6kΩ±50%	11kΩ±50%	16kΩ±50%
Feedback Linearity	Less than 2.00%		
Input Voltage	0-15 VDC. Rated at 12VDC.		
Stall Current	650mA @ 12V		
Operating Temperature	-10°C to +50°C		
Audible Noise	60dB @ 45cm		
Ingress Protection	IP-54		
Mechanical Backlash	0.25mm		
Limit Switches	Max. Current Leakage: 8uA		
Maximum Static Force	250N		
Maximum Duty Cycle	20%		

Figure 2.19. Firgelli L-16 P-Series Linear Electric Actuator Datasheet..

A SolidWorks model is developed to design the wing of the aircraft with the moving-mass actuator mechanism installed in it. The build material of the aircraft is Balsa wood with 159.99 kg/m3 for the internal structure, sheeting and carbon fiber for the spar (Leading edge, Trailing edge and main spar). Figure. 2.20 shows an internal view of the wing which consists of the actuator mechanism, the control board installed and the lead mass. The actuator is equipped with a Lead mass (see Fig. 2.21) placed at its end which will be moving within the wing with a stroke length of 110mm and highest rate of 32mm/sec.

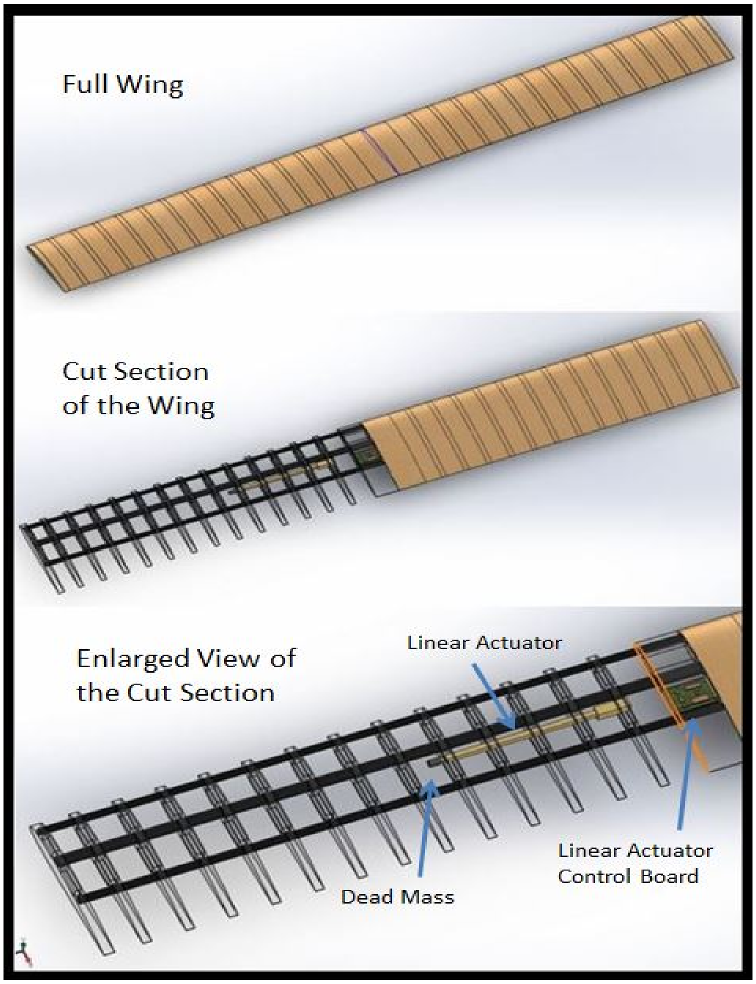

Figure 2.20. Design of the Wings and the Internal Moving-Mass System..

Figure 2.21. Cylindrical Lead Mass for the Actuator.

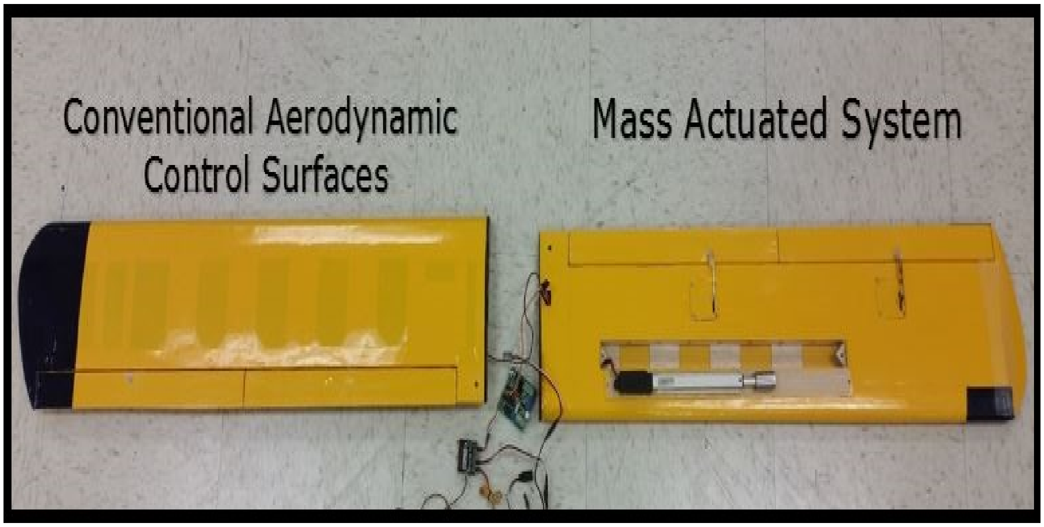

Figure 2.22. Linear Actuators inside the Wing.

2.7 Data Acquisition System

This section describes the layout of the components inside the aircraft and their interface with the Autopilot kit. Pixhawk is the Autopilot unit being used in this study which essentially performs the data logging during flight tests [19]. The linear actuators inside both wings are connected to their respective control boards, which are in turn connected to the Pixhawk.

As mentioned in the previous sections the L-16 P-Series linear actuators are equipped with position feedback system. This would require an additional micro controller like Arduino. Instead the Linear Actuator Control (LAC) Board is connected to pixhawk as a normal PWM signal. The position information is then extracted by the Pixhawk and stored in the data log in terms of PWM's. In addition to the Linear actuators inside the wings for generating the rolling moment, the aircraft is also equipped with conventional aerodynamic control surfaces. These are in order to recover the aircraft in case of any malfunction.

The objective is to operate the aircraft with the moving mass system to create rolling moment. Depending upon the simulation results, the linear actuators will be calibrated with respect to their speed, endpoint adjustment and sensitivity to achieve satisfactory rolling maneuver. The PWM readings from the pixhawk of the linear actuator are converted into their deflection based upon their minimum and maximum PWM values in order to have a brief understanding of the actuation, though this one to one mapping is not completely accurate due to actuator response delay. These components with the autopilot system will be controlled by a 2.4 GHz Radio Transmitter (Futaba T8FG Super) [20]. This is a 14 channel transmitter with variable control ports. The conventional aerodynamic surfaces will be connected to the basic controls of the transmitter. While the Linear Actuator control boards will be connected to the variable control ports on the transmitter with which we can control the position of the mass actuators throughout their stroke length of 110 mm as shown in Fig. 2.23.

Figure 2.23. Futaba T8FG Super with variable control ports.

The layout of the components inside the aircraft are illustrated in Figs. 2.24.

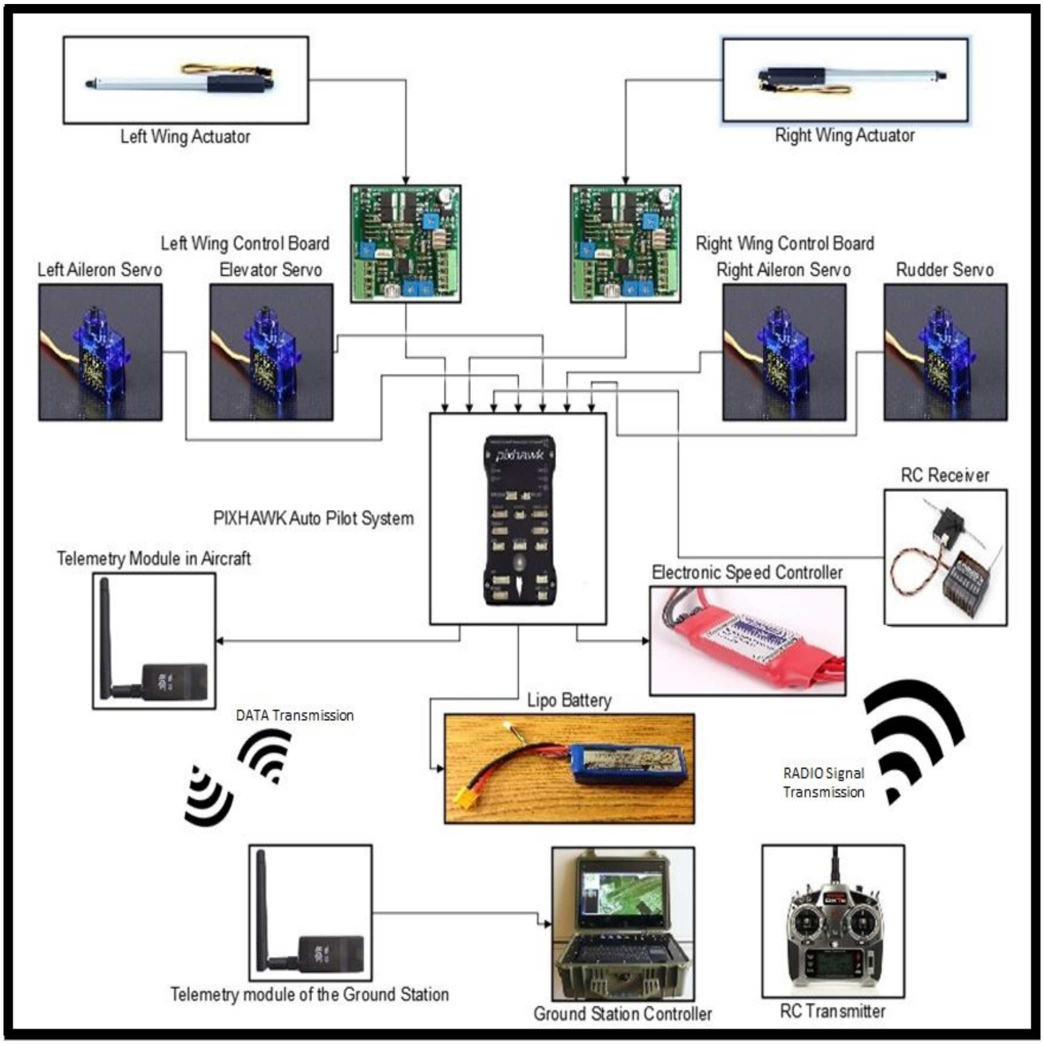

Figure 2.24. Interaction of electronics onboard with Pixhawk.

CHAPTER 3

Modelling and Simulation of the Aircraft

3.1 Equations of Motion

Standard equations of motion with fixed center of mass and inertia cannot be utilized for this study since we require movement of masses within airplane. These equations of motion are obtained by simplifying the equations in Ref. [21]. The equations of motion utilized for this study are from [8], [9], [10], and are presented here for ease of reference. These will be the base for the simulation analysis conducted. The mass actuation simulations are modified for two mass actuation configuration for this study from the single mass actuation model in the reference study. This section describes formulation for representing the Case-1 and Case-2 configurations as explained in Section 3.2.2. Simulation analysis, particularly the trim analysis, is carried out prior to flight test to ensure that the selections of the electric motor and the moving-mass mechanism are adequate for the airplane design. The simulation results are also used to decide the types of flights test to be conducted.

3.1.1 Kinematics

The translational kinematic equation written in matrix form is [21]

$$\dot{\xi} = \mathbf{R}_{\mathbf{B_R I}}^{\mathbf{T}} \mathbf{R}_{\mathbf{B_R W_R}} U \tag{3.1}$$

where $\mathbf{R}_{\mathbf{B_R W_R}}, \mathbf{R}_{\mathbf{B_R I}}$ are the rotation matrices between reference frames, $U = [V\ 0\ 0]^T$ and V is airspeed.

Standard rotational kinematics in terms of Euler angles is used:

$$\dot{\psi} = (q \sin\phi + r \cos\phi) \sec\theta \tag{3.2}$$

$$\dot{\theta} = q \cos\phi - r \sin\phi \tag{3.3}$$

$$\dot{\phi} = p + q \sin\phi \tan\theta + r \cos\phi \tan\theta \tag{3.4}$$

where ψ,θ,ϕ are the euler angles and p, q, r are the components of angular velocity in body frame.

3.1.2 Dynamics

With the simplifications stated in Ref. [8], the translational dynamics equations in Ref. [21] are reduced to

$$\begin{aligned} \dot{\chi} &= \epsilon_R^{-1}[\mathbf{S}(\omega_{\mathbf{B_R I}})](\mathbf{R_{B_R W_R}} U) + \frac{1}{M+m}\epsilon_R^{-1}[\mathbf{R_{B_R I}} F] \\ &- \frac{1}{M+m}\epsilon_R^{-1}\sum_{j=1}^{k}(m_j[\ddot{\rho}_{m_j} + \mathbf{S}(\omega_{\mathbf{B_R I}})[\mathbf{S}(\omega_{\mathbf{B_R I}})\rho_{m_j} - 2\dot{\rho}_{m_j}] + \mathbf{S}(\rho_{\mathbf{m_j}})\dot{\omega}_{B_R I}]) \end{aligned} \tag{3.5}$$

where

$$\chi = \begin{bmatrix} V & \beta & \alpha \end{bmatrix}^T \tag{3.6}$$

and note that ρ_{m_j}, $\dot{\rho}_{m_j}$ and $\ddot{\rho}_{m_j}$ represent position, velocity and acceleration, respectively, of moving-mass actuator m_j relative to the body frame. Similarly, with the simplifications stated in Ref. [8], the rotational dynamics equations in Ref. [21] are reduced to

$$
\begin{aligned}
\dot{\omega}_{B_R I} \;&=\; \underline{\mathbf{I}}_{\mathbf{t}}^{\mathbf{-1}} M_{B_R} + \underline{\mathbf{I}}_{\mathbf{t}}^{\mathbf{-1}} \mathbf{S}(\omega_{\mathbf{B_R I}}) \underline{\mathbf{I}}_{\mathbf{M}} \omega_{B_R I} + \underline{\mathbf{I}}_{\mathbf{t}}^{\mathbf{-1}} \sum_{j=1}^{k} \mathbf{S}(\rho_{\mathbf{m_j}}) \Big[m_j (\omega_{B_R I}^T) \rho_{m_j} (\omega_{B_R I}) + m_j \ddot{\rho}_{m_j} \Big] \\
&+\; \underline{\mathbf{I}}_{\mathbf{t}}^{\mathbf{-1}} \sum_{j=1}^{k} \mathbf{S}(\rho_{\mathbf{m_j}}) m_j \Big[-\mathbf{S}(\omega_{\mathbf{B_R I}}) (\mathbf{R_{B_R W_R}} U) + \epsilon_R \dot{\chi}_R \Big] \\
&-\; 2\underline{\mathbf{I}}_{\mathbf{t}}^{\mathbf{-1}} \sum_{j=1}^{k} m_j [(\rho_{m_j}^T \dot{\rho}_{m_j}) I_{3X3} - \dot{\rho}_{m_j} \rho_{m_j}^T](\omega_{B_R I}) \qquad (3.7)
\end{aligned}
$$

where

$$
\omega_{B_R I} = \begin{bmatrix} p & q & r \end{bmatrix}^T \qquad (3.8)
$$

3.1.3 Applied Forces and Moments

In this study, the aerodynamics and propulsion (electric driven propeller) details of an RC airplane given in the earlier section are used. The direction of the propeller spin axis passes through the origin of the body frame. Further, the origin of the body frame is at the center of mass of the airplane without the moving-mass actuators, which implies no gravitational moment by the aircraft mass. However, the moving-mass actuators produce both gravitational forces and moments. In fact, the gravitational moment by the moving-mass actuators is the mechanism for alternative moment-generation.

The lift and drag coefficients are

$$
C_L = C_{L_0} + C_{L_\alpha} \alpha + C_{L_{\delta_e}} \delta_e + \frac{c}{2V} (C_{L_q} q + C_{L_{\dot{\alpha}}} \dot{\alpha}) \qquad (3.9)
$$

$$
C_D = C_{D_{\delta_e}} \delta_e + C_{D_{\delta_r}} \delta_r + C_{D_{\delta_a}} \delta_a + K_2(\beta) \alpha^2 + K_1(\beta) \alpha + K_0(\beta) \qquad (3.10)
$$

where the last three terms of C_D expression are added to model the contribution of side slip angle on drag. The coefficients K_2, K_1 and K_0 are second order polynomials of β and determined based on experimental data of a micro air vehicle [22]. Table. 3.1 consists of the aerodynamic coefficients for the aircraft. These are calculated from the mathematical formulas from Ref. [23] and also based on data of some other aircraft with similar profile, available in Refs. [24] and [25].

Table 3.1. Aerodynamic Coefficients of the Aircraft

Parameter	Reading
C_{L_0}	0.28
C_{L_α}	5.65
$C_{L_{\delta_e}}$	0.22
C_{L_q}	7.5
$C_{D_{\delta_e}}$	-0.0046
$C_{D_{\delta_r}}$	0.37442
$C_{D_{\delta_a}}$	0.374
C_{Y_β}	-0.2595
$C_{Y_{\delta_r}}$	0.1584
C_{y_p}	0.0075
C_{y_r}	0.146
C_{l_β}	-0.9
$C_{l_{\delta_a}}$	0.1519
$C_{l_{\delta_r}}$	0.0042
C_{l_p}	-0.65596
C_{l_r}	0.18415
C_{m_0}	0.048
C_{m_α}	-0.473
$C_{m_{\delta_e}}$	-1.262
C_{m_q}	-16.479
$C_{m_{\dot\alpha}}$	-4.7
C_{n_β}	0.04641
$C_{n_{\delta_a}}$	-0.0139
$C_{n_{\delta_r}}$	-0.0465
C_{n_p}	-0.04016
C_{n_r}	-0.0358

Aerodynamic forces and moments coefficients in the body frame are

$$C_X = C_L \sin\alpha - C_D \cos\alpha \tag{3.11}$$

$$C_Y = C_{Y_\beta}\beta + C_{Y_{\delta_r}}\delta_r + \frac{b}{2V}(C_{y_p}p + C_{y_r}r) \tag{3.12}$$

$$C_Z = -C_L \cos\alpha - C_D \sin\alpha \tag{3.13}$$

$$C_l = C_{l_\beta}\beta + C_{l_{\delta_a}}\delta_a + C_{l_{\delta_r}}\delta_r + \frac{b}{2V}(C_{l_p}p + C_{l_r}r) \tag{3.14}$$

$$C_m = C_{m_0} + C_{m_\alpha}\alpha + C_{m_{\delta_e}}\delta_e + \frac{c}{2V}(C_{m_q}q + C_{m_{\dot\alpha}}\dot\alpha) \tag{3.15}$$

$$C_n = C_{n_\beta}\beta + C_{n_{\delta_a}}\delta_a + C_{n_{\delta_r}}\delta_r + \frac{b}{2V}(C_{n_p}p + C_{n_r}r) \tag{3.16}$$

Then, the aerodynamic forces and moments are calculated as

$$X = C_X QS \tag{3.17}$$

$$Y = C_Y QS \tag{3.18}$$

$$Z = C_Z QS \tag{3.19}$$

$$\mathcal{L} = C_l QSb \tag{3.20}$$

$$\mathcal{M} = C_m QSc \tag{3.21}$$

$$\mathcal{N} = C_n QSb \tag{3.22}$$

For mass actuation analysis, the terms of the aerodynamic control surfaces in the aerodynamic model are set to zero. The components of the gravitational forces in the body frame, due to the aircraft mass and moving-mass actuators, are

$$\begin{bmatrix} G_x \\ G_y \\ G_z \end{bmatrix} = \mathbf{R_{B_RI}} \begin{bmatrix} 0 \\ 0 \\ m_T g \end{bmatrix} \tag{3.23}$$

where

$$m_T = M + \sum_{j=1}^{k} m_j \tag{3.24}$$

The components in the body frame of the gravitational moments due to the moving-mass actuators are

$$\begin{bmatrix} \mathcal{L}_{mass} \\ \mathcal{M}_{mass} \\ \mathcal{N}_{mass} \end{bmatrix} = -\sum_{j=1}^{k} S(\rho_{m_j}) \mathbf{R_{B_R I}} \begin{bmatrix} 0 \\ 0 \\ m_j g \end{bmatrix} \tag{3.25}$$

where $S(\rho_{m_j})$ is the skew-symmetric matrix of the representation of the position of the jth moving mass, which is written in body frame, as

$$\rho_{m_j} = \begin{bmatrix} \rho_{m_{j_x}} & \rho_{m_{j_y}} & \rho_{m_{j_z}} \end{bmatrix}^T \tag{3.26}$$

Furthermore, propulsion dynamics is represented with typical DC Motor equations [26, 27, 28, 29] based on properties of electric motor, propeller and battery stated in Ref. [8] as

$$\dot{i} = \frac{1}{L} \left[-Ri - k_e \omega_p + \mathcal{V}_s \right] \tag{3.27}$$

$$\dot{\omega}_p = \frac{1}{J_p + J_m} \left[k_T i - k_f \omega_p - \tau_p(\omega_p, V) \right] \tag{3.28}$$

where propeller torque, τ_p, is calculated based on APC 11 x 6E propeller data [30] by setting up a interpolation function for given airspeed, V, and propeller angular speed, ω_p. Thrust generated by the propeller is also calculated from the same propeller data for aircraft speed, V, and propeller angular speed, ω_p. Hence, thrust and propeller torque equations are the functions of these terms and can be written as

$$T = f(\omega_p, V) \tag{3.29}$$

$$\tau_p = f(\omega_p, V) \tag{3.30}$$

Since the direction of the propeller spin axis is along the x-axis of the body frame, the propeller thrust is assumed to be along the x-axis and the propeller torque is only around the x-axis.

Final form of the applied force and moment expressions are

$$F_{B_R} = \begin{bmatrix} X + T_x + G_x \\ Y + T_y + G_y \\ Z + T_z + G_z \end{bmatrix} \tag{3.31}$$

$$M_{B_R} = \begin{bmatrix} \tau_{p_x} + \mathcal{L} + \mathcal{L}_{mass} \\ \tau_{p_y} + \mathcal{M} + \mathcal{M}_{mass} \\ \tau_{p_z} + \mathcal{N} + \mathcal{N}_{mass} \end{bmatrix} \tag{3.32}$$

These equations of motion along with the trim analysis results from [11] are used for the mass actuation study with further development. In the following section, trim analysis are carried with varying airspeed and the trim results are presented. The goal in this study is to determine the feasible speed range for the aircraft and also to determine whether the mass-actuation can maintain the aircraft in a desired trim condition (cruise or steady-turn) with a given airspeed.

3.2 Simulation Cases

This section discusses the modeling of different mass actuation setups employed in this study. The actuation system employed in Ref. [11] consists of a single mass moving throughout the wing performing mass actuation in the lateral direction. The maximum stress on the aircraft wing is at its root and especially at the wing mounting section. In practical implementation, if we have a hollow section at the root of the wing for a mass to travel from one end to other, the wing will loose its strength. Also installing a mechanism to fit inside the wing section which can travel a single piece of mass from one end to other within 1 inch of thickness (as in our case) is a complex task. Hence, this arrangement is difficult to implement in a small Unmanned Aerial Vehicle. This leads to the choice of having two actuators; one in each wing carrying one mass. With this configuration, the aircraft can perform the desired mass actuation task while still maintaining its structural strength.

In the case of single mass that can move from the tip of one wing to that of the other wing, the shift in the center of mass of the whole aircraft (ρ_{cmy}) is calculated. The case with one mass in each wing should lead to the same total center of mass shift. This can be achieved in two different cases: (1) one mass stays at its most retracted position while the mass in the other wing extends such that the same total center of mass shift is achieved, and (2) both masses start at the middle of their respective motion range, and move simultaneously to the left or right to achieve the same total center of mass shift.

All the simulation cases analyzed below are with the propeller torque and without rudder deflection. This results in side slip angle and non-zero aileron or lateral mass placement even in the case of cruise condition. The Elevator - Aileron configuration is labeled as A/C - 1 and the Elevator - Lateral Mass configuration is labeled as A/C - 2.

3.2.1 Elevator and Aileron Configuration

This section consists of the standard aircraft configuration without the mass actuation system. This particular setup is considered without rudder deflection and consists of only elevator and aileron deflection. Presented below are the endurance, range, elevator deflection, aileron deflection and roll angle (ϕ) plots of the A/C - 1 in Fig. 3.1 - Fig. 3.5, respectively.

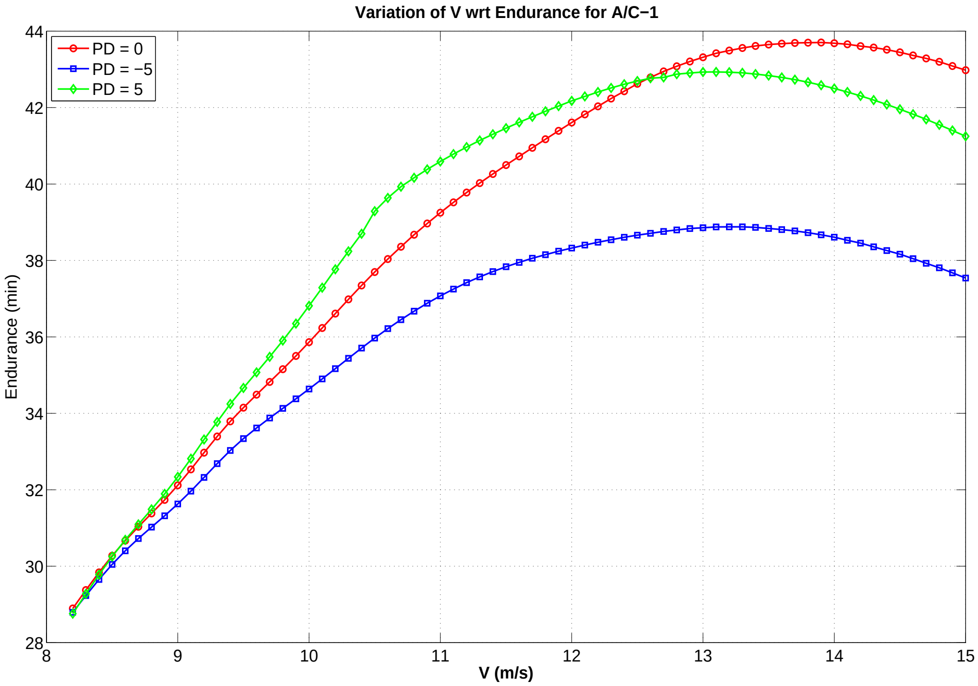

Figure 3.1. Endurance.

The endurance plot in Fig. 3.1 shows similar trends for cruise, right turn and left turn flights with difference in their limits. The overall highest endurance logged is during the cruise condition with an endurance of 43 mins approximately. This limit is attained at a velocity of 13.8 m/sec.

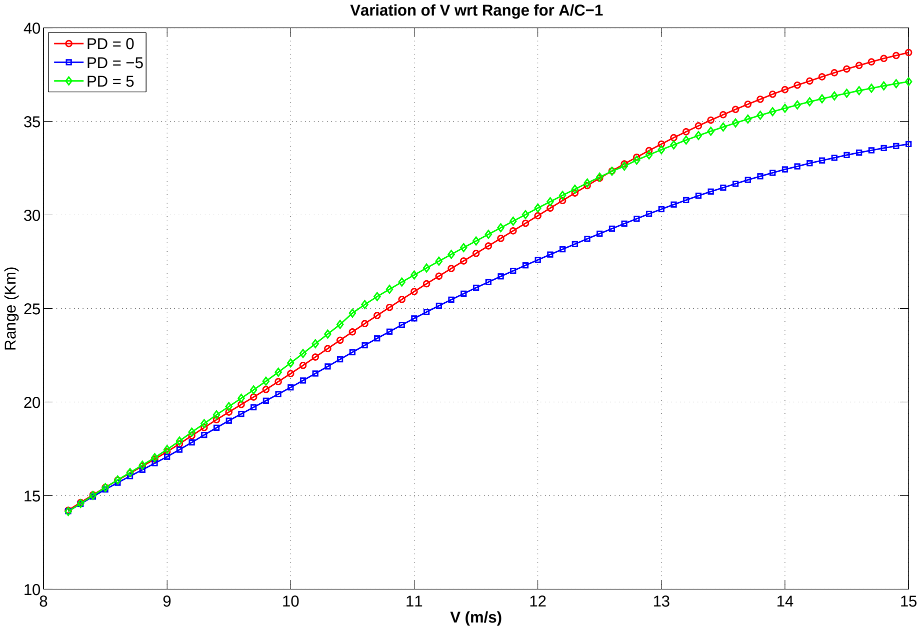

Figure 3.2. Range.

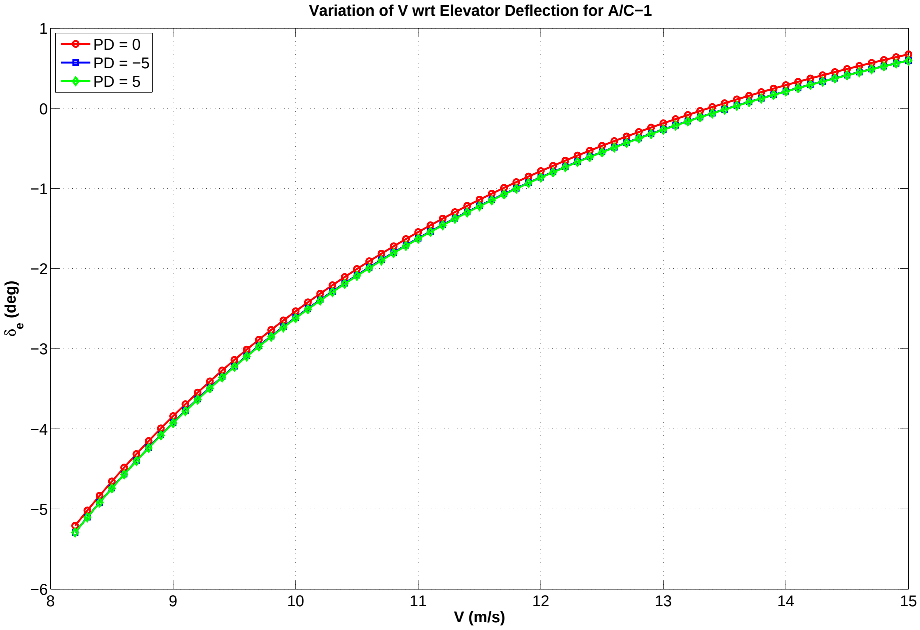

Figure 3.3. Elevator Deflection.

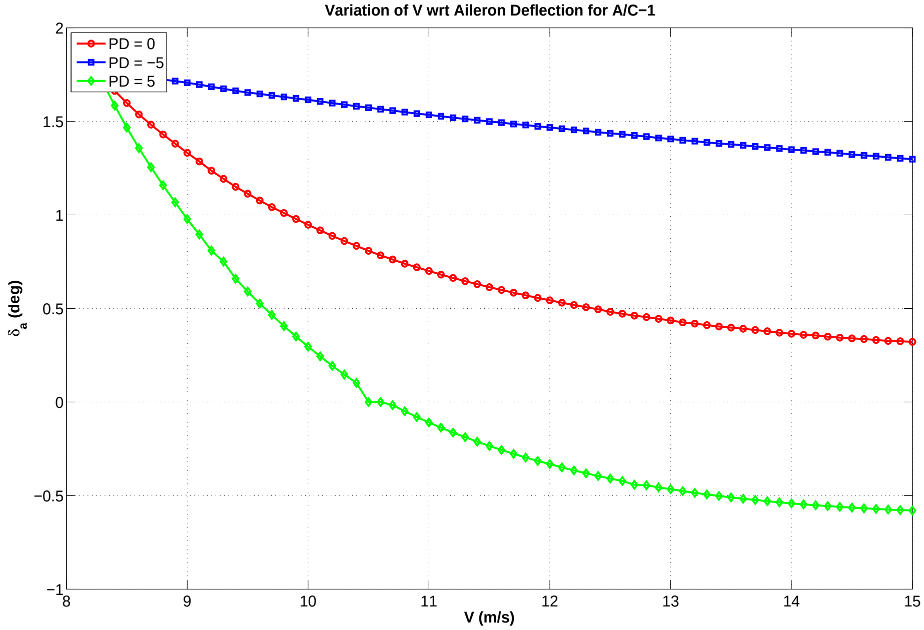

Figure 3.4. Aileron Deflection.

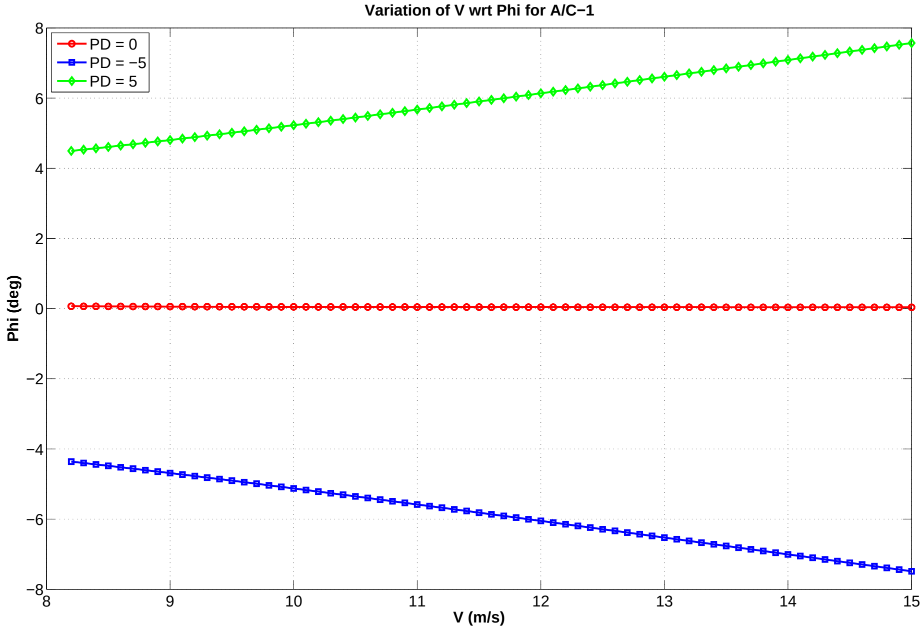

Figure 3.5. Roll Angle.

The range plot in Fig. 3.2 again shows similar trends for cruise, right turn and left turn flights with difference in their limits as in the case of the endurance. The overall highest range logged is during the cruise condition with a range of more than 38 km approximately. These values of maximum range and endurance will be later discussed in the further sections in comparison to the mass actuated airplanes results.

With the given set of control inputs for a 5 degrees/sec turn rate within the allotted speed range, the aircraft produces a maximum and minimum of + 8 degrees to - 8 degrees roll angle, respectively, as can be seen in Fig. 3.5.

3.2.2 Elevator and Lateral Masses Configuration

This configuration consists of elevator for longitudinal control, lateral masses for the lateral control of the aircraft and with zero rudder. The mass actuation with this configuration is further divided into two sections. Depending upon the capabilities of the Linear Actuator used in the aircraft, the mass actuation in the lateral direction can be performed in two different ways, as discussed earlier:

1) Case 1: Two Internal Moving-Masses in either wing moving alternately; and

2) Case 2: Two Internal Moving-Masses in either wing moving simultaneously.

Figure. 3.6 depicts these case. In the representation below, the red dot depicts the initial position of the masses. The green bar represents the ρ_{min} (the most retracted position) and red bar ρ_{max} (the most extracted position). The initial position of the masses inside either wings is at ρ_{min}, which is 35 cm from the center of the wing and the actuator has a stroke length of 11cms making the ρ_{max} as 46 cm from the center of the wing. As we observe in the picture, in Case 1 both the masses remain at the ρ_{min} in either side. During right actuation the mass in the left wing remains at -ρ_{min}, while the right mass is moved towards its ρ_{max}. Similarly, during the left mass actuation the right mass remains at its ρ_{min} and the left mass moves to its - ρ_{max}. In Case 2 both the masses are extended to their half throws (5.5 cm on either side from ρ_{min}). During the right mass actuation the right actuator moves from + 40.5 cm to the ρ_{max} and the left mass moves from - 40.5 cm to its - ρ_{min} and vice versa creating a simultaneous motion of masses.

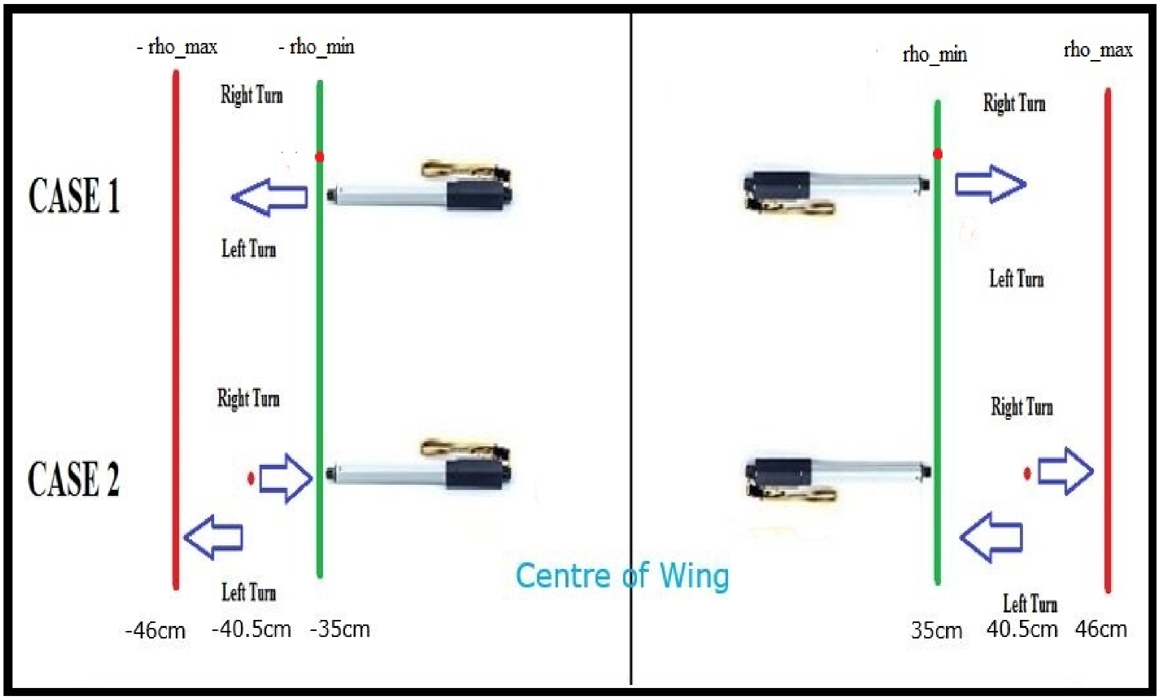

Figure 3.6. Mass Actuation Configurations.

Given the ρ_{m2y} (position of the moving mass in the case of single mass moving from wing tip to wing tip), the ρ_{cmy} (center of mass) of the whole aircraft is calculated as:

$$m_2\rho_{m2y} = m_t\rho_{cmy} \tag{3.33}$$

$$\rho_{cmy} = (\frac{m_2}{m_t})\rho_{m2y} \tag{3.34}$$

where m_2 is the mass of the single moving mass, and m_t is the total aircraft mass.

From this ρ_{cmy} calculation of the whole aircraft which has a single mass actuation in the lateral direction, our two mass actuation model can be developed. The boundary conditions for the Case 1 configuration where the left mass ρ_1 remains at - ρ_{min} during right mass actuation ($\rho_{cmy} \geq 0$) and the right mass remains at ρ_{min} during the left mass actuation ($\rho_{cmy} \leq 0$) respectively.

if $\rho_{cmy} \geq 0$ the boundary condition (right mass actuation) is:

$$\rho_1 = -\rho_{min} \tag{3.35}$$

substituting this in the total moment equation gives

$$m_t\rho_{cmy} = m_2\rho_1 + m_2\rho_2 \tag{3.36}$$

$$\rho_2 = \frac{1}{m_2}(m_t\rho_{cmy} + m_2\rho_{min}) \tag{3.37}$$

$$\rho_2 = (\frac{m_t}{m_2})\rho_{cmy} + \rho_{min} \tag{3.38}$$

where m_2 is the lateral mass on either side of the wing.

When $\rho_{cmy} \leq 0$ is the boundary condition (left mass actuation):

$$\rho_2 = \rho_{min} \tag{3.39}$$

substituting ρ_2 value in the total moment equation gives

$$m_t\rho_{cmy} = m_2\rho_1 + m_2\rho_2 \tag{3.40}$$

$$\rho_1 = \frac{1}{m_2}(m_t\rho_{cmy} - m_2\rho_{min}) \tag{3.41}$$

$$\rho_1 = (\frac{m_t}{m_2})\rho_{cmy} - \rho_{min} \tag{3.42}$$

In Case-2, the masses in the left and right wings are initially placed at the middle of their respective range. That is,

$$\rho_1 = -\frac{\rho_{min} + \rho_{max}}{2} \tag{3.43}$$

$$\rho_2 = \frac{\rho_{min} + \rho_{max}}{2} \tag{3.44}$$

where ρ_1 and ρ_2 are the positions of the left and right wing masses, respectively.

In this case, the two masses move simultaneously in the same direction with the same rate when the center of mass of the aircraft is desired. This implies that when the masses are at their most right positions, their positions are

$$\rho_1 = -\rho_{min} \tag{3.45}$$

$$\rho_2 = \rho_{max} \tag{3.46}$$

Similarly, when the masses are at their most left positions,

$$\rho_1 = -\rho_{max} \tag{3.47}$$

$$\rho_2 = \rho_{min} \tag{3.48}$$

Using these boundary conditions in the moment equations for calculating the center of mass, the positions for the two masses are calculated as functions of a given center of mass position for the whole aircraft as

$$\rho_2 = \frac{1}{2}[\frac{m_t}{m_2}\rho_{cmy} + \rho_{min} + \rho_{max}] \tag{3.49}$$

$$\rho_1 = \rho_2 - (\rho_{min} + \rho_{max}) \tag{3.50}$$

Trim analysis as developed for the single mass moving along the span of the whole wing from Ref. [12] is used along with the expressions in equations (3.49) and (3.50) to calculate the required left and right mass positions.

As in the case of standard aircraft, the mass actuated aircraft trim analysis is carried out in cruise, left and right steady-turn cases. The turn rate, as before, is 5 deg/s. The trim analysis is repeated in each case for varying desired airspeed. Figs. 3.7 and 3.8 show the endurance and range, respectively.

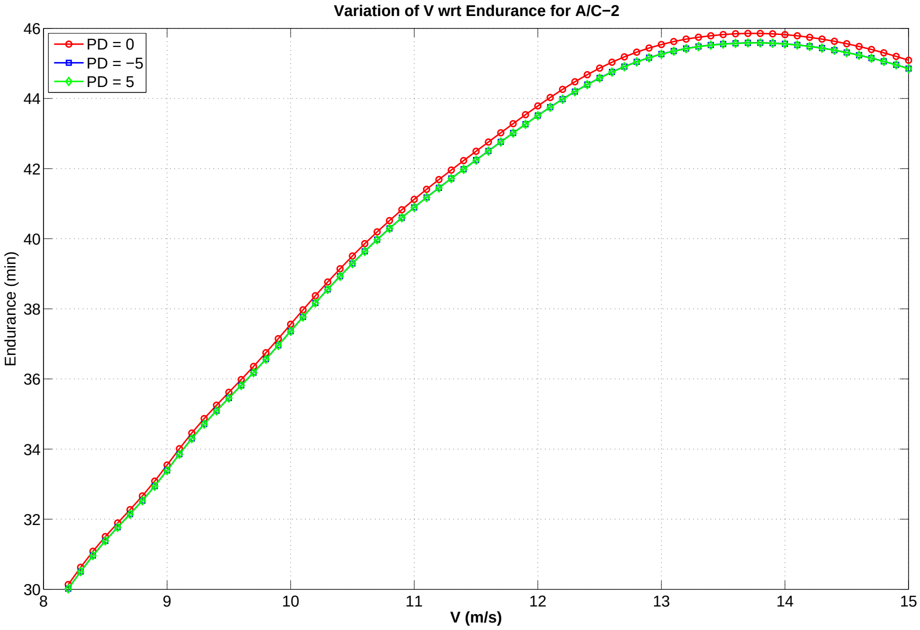

Figure 3.7. Endurance.

The endurance plot in Fig. 3.7 shows similar trends for cruise, right turn and left turn flights. The overall highest endurance logged is during the cruise condition with an endurance of 46 mins approximately. This limit is attained at a velocity of 13.8 m/sec.

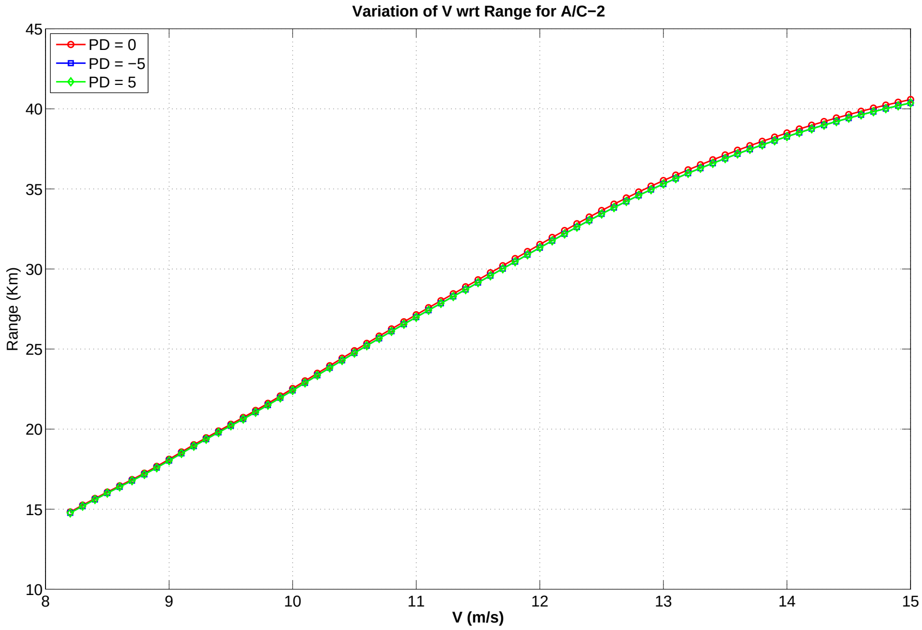

Figure 3.8. Range.

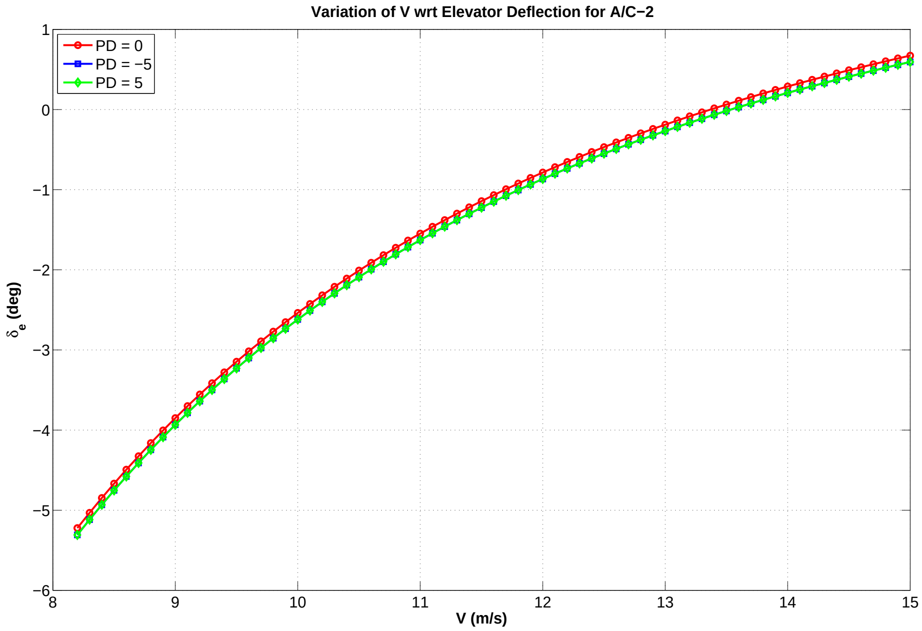

Figure 3.9. Elevator Deflection.

The range plot in Fig. 3.8 again shows similar trends for cruise, right turn and left turn flights as in the case of the endurance. The overall highest range logged is during the cruise condition with a range of more than 41 km approximately. These results may vary slightly with different or higher speed ranges and turn rates. The range and endurance analysis in the given speed range show maximum outputs in 15m/sec and 13.8 m/sec approximately. An evaluation of the endurance and range produced by both conventional aerodynamic surfaces and mass actuated system is performed.

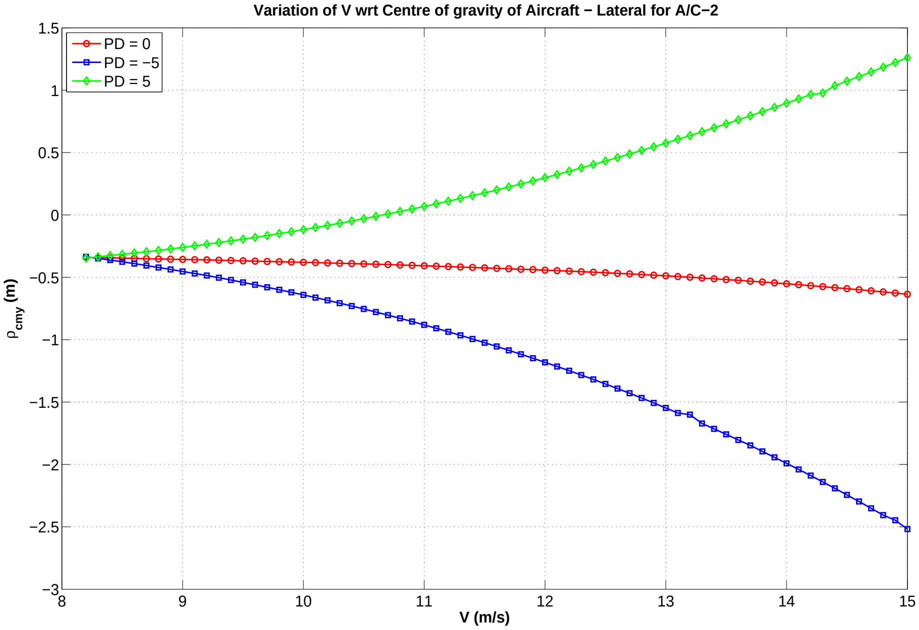

Figure 3.10. ρ_{cmy} of the total aircraft.

The results show an increase of 3 mins in the endurance and 3 km of range approximately in comparison to conventional aerodynamic surfaces. In this analysis the total weight of the aircraft remains constant. With the constant weight condition, the feasibility and advantage of the mass actuated systems over the conventional aerodynamic surfaces is demonstrated. The maximum range obtained is about 41 km and the maximum endurance is 46mins.

Figure. 3.10 shows the required shift in center of mass of the total aircraft in the lateral direction to maintain the desired flight condition, i.e., to fly with the desired airspeed and turn rate, or zero turn rate in the case of cruise. For the required total aircraft center of mass position from Fig. 3.10, the expressions developed earlier for the two cases of mass motion configurations are used to calculate the required mass positions in the left and right wings. Fig. 3.11 shows the left and right mass position variation for Case 1 (only one mass moves at a time while the other stays at the most retracted position), and Fig. 3.12 shows the Case 2 (masses nominally stay in the middle of their feasible ranges and move simultaneously in the same direction).

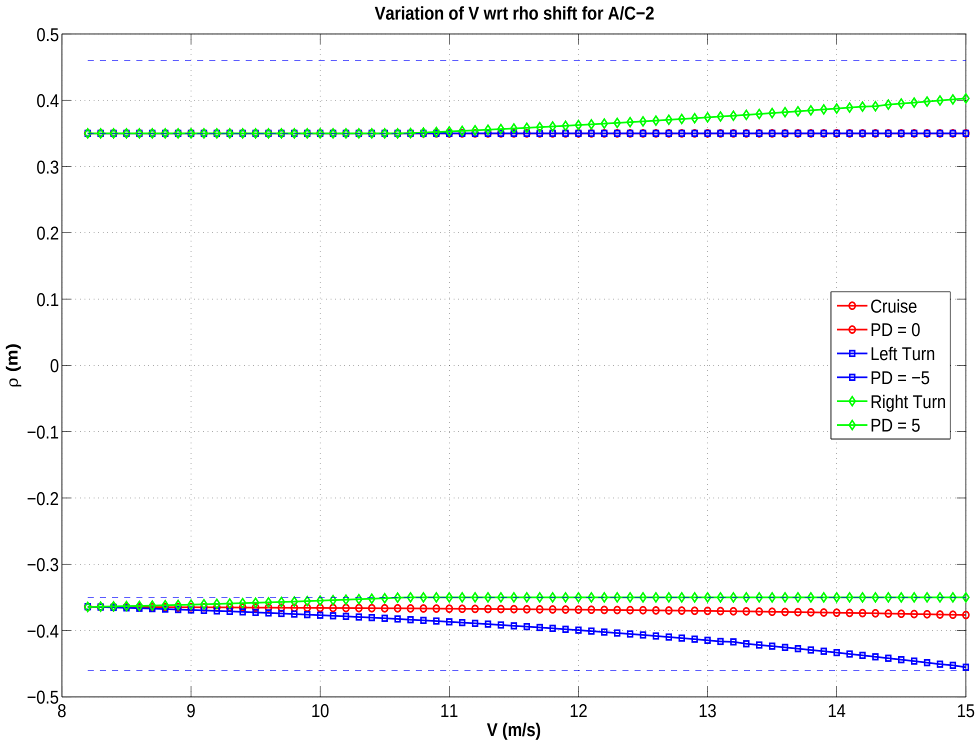

Figure 3.11. Case 1 Configuration Mass Shift.

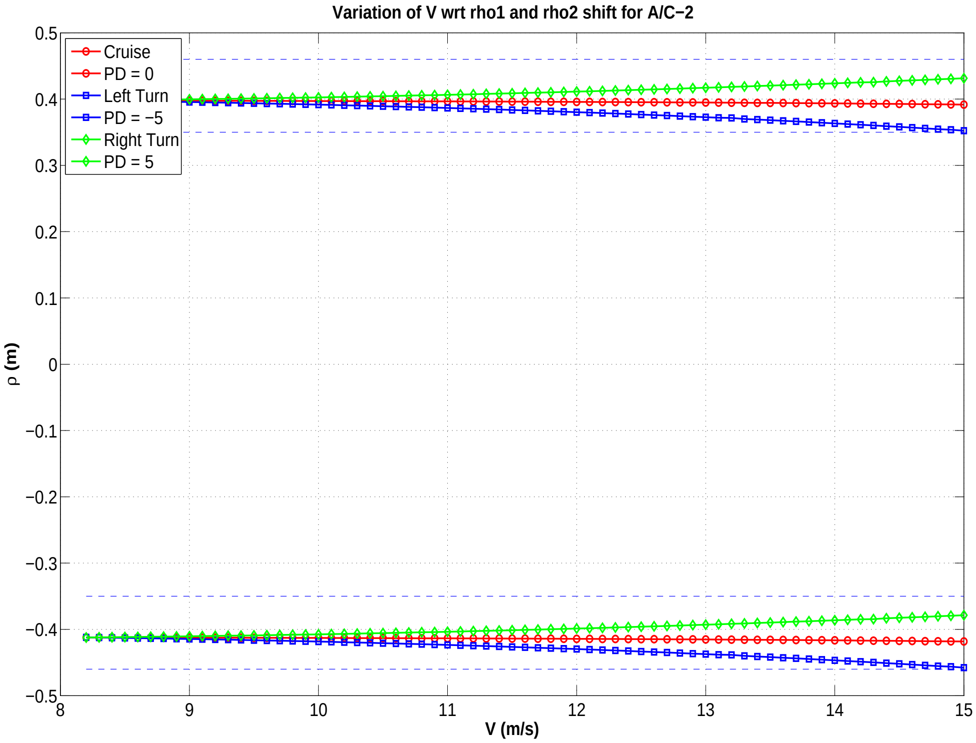

Figure 3.12. Case 2 Configuration Mass Shift.

Figures. 3.11 and 3.12 for ρ_1 and ρ_2 shifts show that the desired turn rate can be achieved within the permissible limits of the actuator. It is seen that the right turn is achieved with a significant amount of buffer left for the mass to shift more within its limits. The left turn is possible only till 15m/sec. Another observation made here is that both configurations, Case 1 and Case 2, produce the same results, i.e, they have the same cutoff speeds for both right and left turn actuation. Also, the maximum range and endurance fall within the speed ranges of the actuator depicting their possibility of generating 5 deg/sec turn rate in implementation.

Since the both configurations have shown identical feasible results for the given turn rate, the next question to be answered is which configuration should be used in the actual implementation. To answer this question, the concept resorted is the relation between roll rate p and inertia I_{xx}. From the rotational dynamics in Eq. (3.7), it can be shown, in the most simplified form, that given the applied moment, the roll rate generated is inversely proportional to the moment of inertia around the x-axis, i.e.,

$$p \approx \frac{M}{I_{xx}} \tag{3.51}$$

As illustrated in Fig. 3.6, the distances of the masses to the centerline for a given desired total center of mass position shift are smaller in Case 1 as compared to those in Case 2. This implies that the I_{xx} for Case 1 would be smaller than Case 2 and hence would produce higher roll rate. Therefore, Case 1 configuration is chosen for the real time implementation on the Unmanned Aerial Vehicle.

CHAPTER 4

Test Flight

4.1 Procedure of Flight Test and Data Acquisition

The aircraft was tested for mass actuation at a safe altitude with constant throttle. While performing a particular turn, the actuator is extended to its limit using the variable control input ports on the transmitter. During the actuation process, the aileron control is untouched and once the mass actuator creates a significant amount of roll angle, elevator actuation is performed to complete a level turn. Once the turn is completed, the aircraft is leveled back to neutral using the control surfaces. Current experimental results provided below is with a single mass of 70 gm in each wing with a total takeoff weight of 3.0 kg.

During the flight test the data acquisition system is logging all the aircraft control inputs, GPS data and various other sensor data in the pixhawk. The pixhawk stores these log files in the form of bin files in the memory card. Through Mission Planner, these bin files are converted into dot mat files, which is a file type that can be read into Matlab environment. Mission Planner is the Graphical User Interface (GUI) of the Pixhawk AutoPilot System. The following are the analyzed data of the flight which show mass actuation results.

Figure. 4.1 are the Google Earth flight path images which show the total flight sketch over the field followed by the Longitude - Latitude plotting. While looking at the Latitude-Longitude plot in Fig. 4.2, the wind direction is represented by an arrow mark and, as we observe, both turns start in the tail wind and level up back into the head wind.

Figure 4.1. Google Earth Flight Path.

Figure 4.2 illustrates the flight path and the mass actuated turns. The green square and red square represent the take-off and landing points, respectively. The series of points on the flight path depict the mass actuated turns. The green points represent right mass actuated turn and black points represent left mass actuated turn. As can be seen, these points have numbers for their respective turns, which show the direction of the turn performed. The turning maneuver in each turn starts at number-1 and ends at number-2. The flight results of the two turns performed are shown in the Flight Test Results Section (4.2). Fig. 4.3 shows the results of the left mass actuated turn, i.e, the black points in Fig. 4.2 and Fig. 4.4 shows the right mass actuated turn, i.e, the green points in Fig. 4.2.

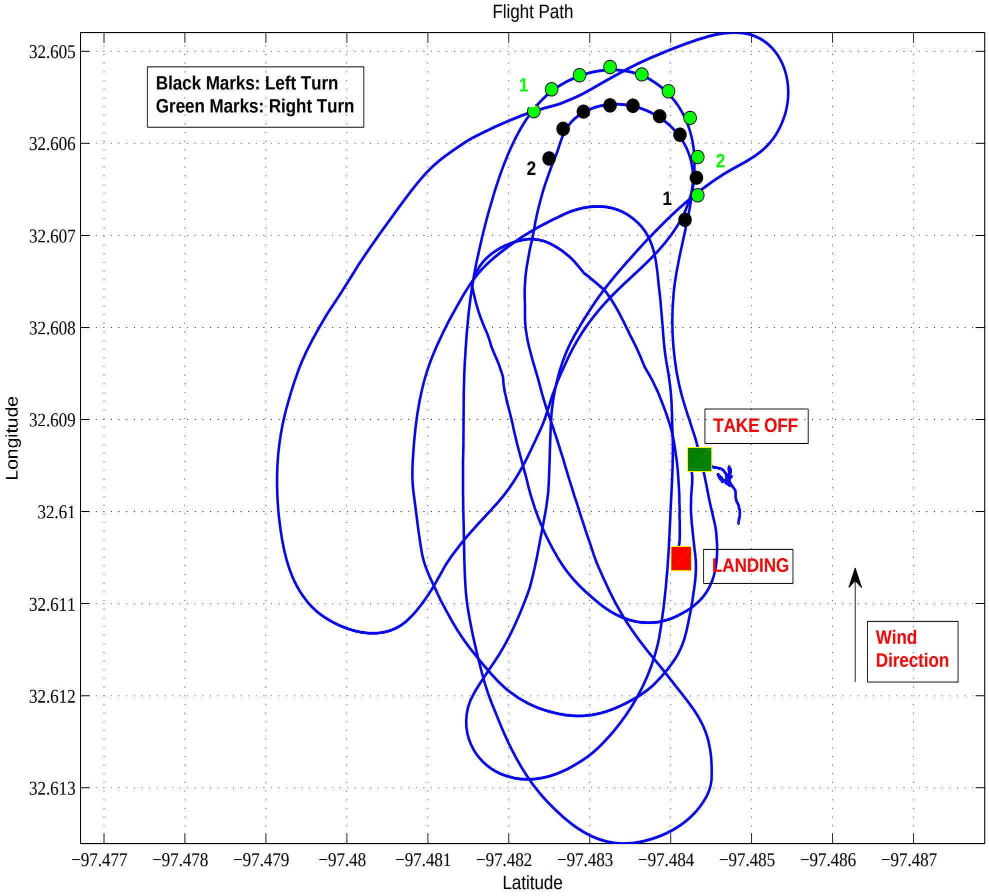

Figure 4.2. Flight Path with Mass Actuation Turns.

4.2 Flight Test Results

During the flight, the left and right turns were performed at almost the same altitude for having better comparison of their results. As described in the earlier discussion, during the mass actuated turn, the aircraft is allowed to dip a particular wing depending upon the turn. Once a particular amount of roll angle is generated due to the masses, gradual elevator input is provided to complete the turn. These actions can be visualized by looking at the results below. LLAC and RLAC labels in the plots below depict the Left Linear Actuator and Right Linear Actuator respectively.

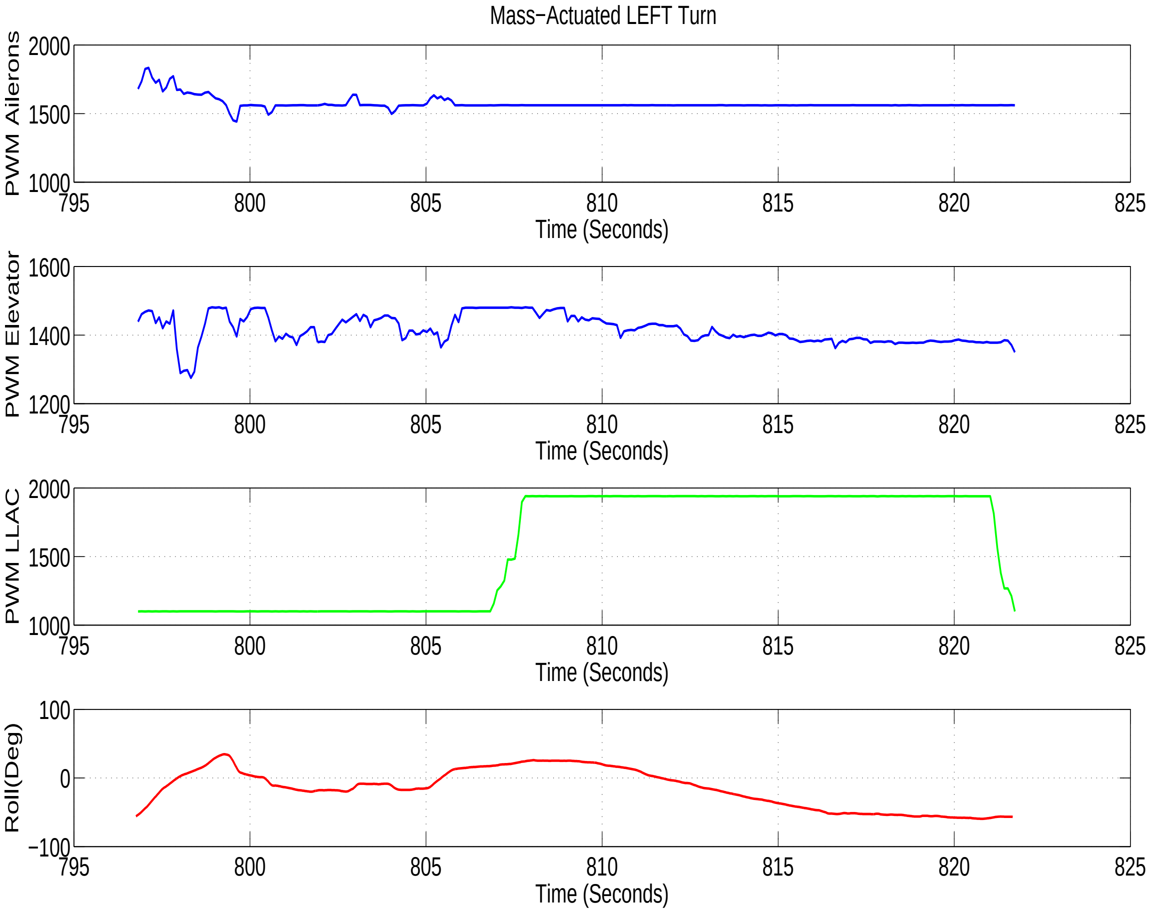

Figure 4.3. Left Turn Results.

As we can see, during the mass actuation, the aileron PWM come to a constant value showing that no aileron input was provided, which indicates zero aileron deflection. Parallel to this, we can also observe the linear actuator's PWM increasing to its highest value as the actuator was extended to its upper limit. Coupled with the linear actuator and aileron PWM, we have the elevator input to perform the required turn. This set of simultaneous control inputs resulted in a significant amount of -60 degrees and + 60 degrees of roll angle generated in either cases. These flight test results demonstrate the effectiveness of the mass actuation in flying the aircraft in steady turn.

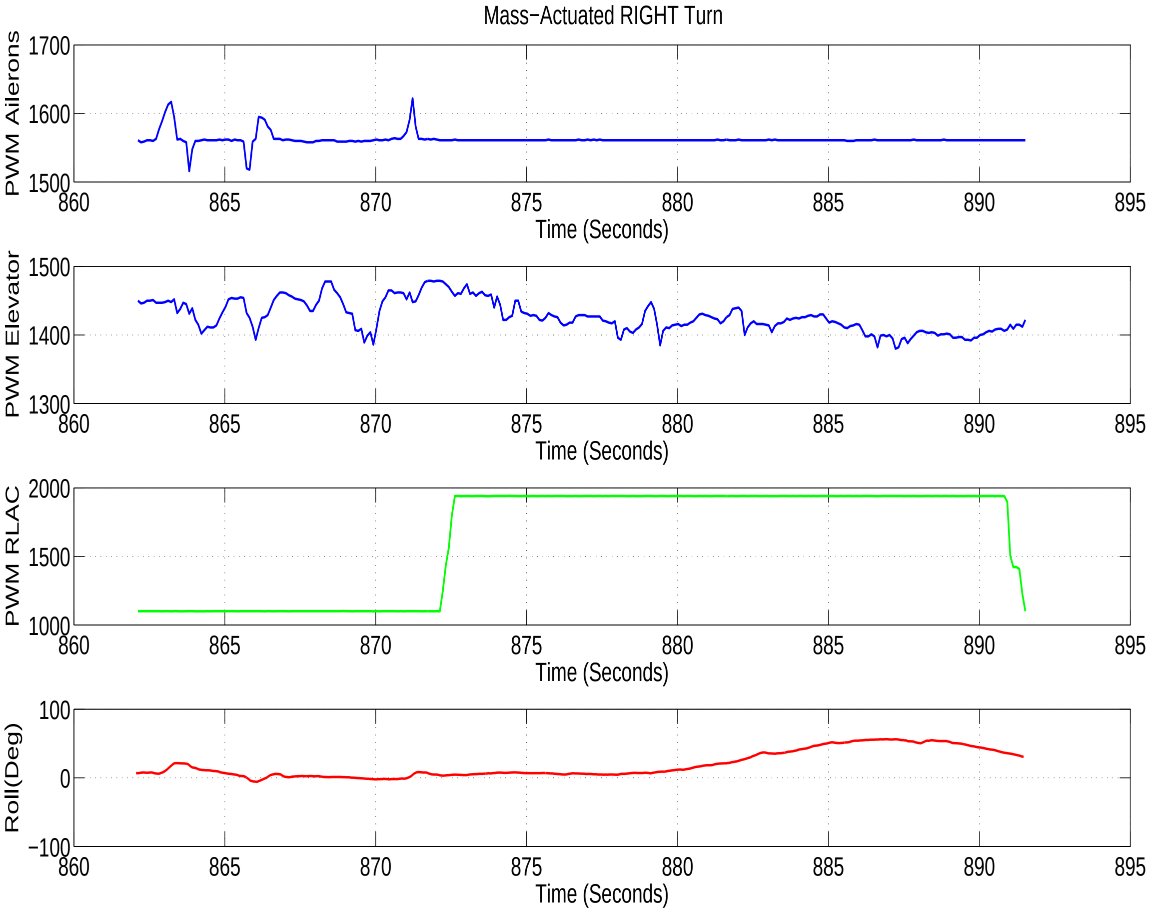

Figure 4.4. Right Turn Results.

CHAPTER 5

CONCLUSIONS AND FUTURE WORK

Simulations prove the feasibility of implementing moving mass actuators instead of conventional control surfaces to generate aerodynamic moments. Flight test results prove that Moving-Mass Actuation system can produce sufficient rolling moment and perform turning maneuvers. The main objective of this research of designing, building and flight testing an Unmanned Aerial Vehicle equipped with mass actuation system to generate rolling moments is accomplished. This work serves as a proof of concept of implementing mass actuation systems to generate required moments in a aircraft during flight.

Future work would be to optimize the existing mass actuation system to perform additional analysis. Calculation of maximum turn rates generated by the system and documentation of their results with different weight configurations. Implementing mass actuation system for both pitching and rolling together to perform level turns should be carried out to have a complete mass-actuated aircraft.

REFERENCES

[1] M. Ross, "Mechanism for precision orbit control with applications to formtation flying," in *AIAA Journal of Guidance, Control, and Dynamics*, vol. 25, no. 4, 2002.

[2] R. H. Byrne, B. R. Sturgis, and R. D. Robinett, "A moving mass trim control system for reentry vehicle guidance," in *AIAA Guidance, Navigation and Control Conference*, 1996, pp. 644 – 650.

[3] S. Wang, M. Yang, and Z. Wang, "Moving-mass trim control system design for spinning vehicles," in *Intelligent Control and Automation, 2006. WCICA 2006. The Sixth World Congress on*, vol. 1, 2006, pp. 1034–1038.

[4] P. Lin and J. Zhou, "Researching variable structure control of moving mass reentry-vehicles," in *Computer Science and Information Technology (ICCSIT), 2010 3rd IEEE International Conference on*, vol. 8, July 2010, pp. 126–129.

[5] P. K. Menon, G. D. Sweriduk, E. J. Ohlmeyer, and D. S. Malyevac, "Integrated guidance and control of moving-mass actuated kinetic warheads," *Journal Of Guidance, Control, And Dynamics*, vol. 27, no. 1, 2004.

[6] S. Tangirala and J. Dzielski, "A variable buoyancy control system for a large auv," *Oceanic Engineering, IEEE Journal of*, vol. 32, no. 4, pp. 762 –771, oct. 2007.

[7] C. Woolsey and N. Leonard, "Moving mass control for underwater vehicles," in *American Control Conference, 2002.*, vol. 4, 2002, pp. 2824–2829.

[8] S. A. Erturk, O. Daskiran, and A. Dogan, “Trim analysis of a moving-mass actuated airplane,” in *AIAA Atmospheric Flight Mechanics Conference*, Minneapolis, MN, 2012.

[9] S. A. Erturk and A. Dogan, “Trim analysis of a moving-mass actuated airplane in steady turn,” in *51st AIAA Aerospace Sciences Meeting including the New Horizons Forum and Aerospace Exposition*, Grapevine, TX, 2013.

[10] ——, “Trimming mass-actuated airplane in turns with zero side slip angle,” in *AIAA Atmospheric Flight Mechanics Conference*, National Harbor, MD, 2014.

[11] ——, “Propeller torque effect on cruise trim of standard and mass-actuated airplane,” in *AIAA Atmospheric Flight Mechanics Conference*, Kissimmee, FL, 2015.

[12] ——, “Propeller torque effect on cruise trim of standard and mass-actuated airplane,” in *AIAA Atmospheric Flight Mechanics Conference*, Dallas, TX, 2015.

[13] “Turnigy d3548/4 1100kv brushless outrunner motor,” http://www.hobbyking.com/hobbyking/store, accessed: 10/25/2015.

[14] “Turnigy plush 60 amps esc,” http://www.hobbyking.com/hobbyking/store, accessed: 10/25/2015.

[15] “Turnigy 5000mah 4s 25c lipo packs,” http://www.hobbyking.com/hobbyking/store, accessed: 10/25/2015.

[16] “Hitec 85mg digital metal gear servo,” http://www3.towerhobbies.com/, accessed: 10/25/2015.

[17] “Adafruit feedback metal gear servo,” https://www.adafruit.com/products, accessed: 10/25/2015.

[18] “Firgelli l-16 p-series linear actuator,” http://store.firgelli.com/, accessed: 09/13/2015.

[19] "Pixhawk autopilot kit," https://store.3drobotics.com/products/3dr-pixhawk, accessed: 09/13/2015.

[20] "Futaba t8fg super transmitter," http://www3.towerhobbies.com/, accessed: 10/25/2015.

[21] J. Waishek, A. Dogan, and W. Blake, "Derivation of the dynamics equations of receiver aircraft in aerial refueling," *Journal of Guidance, Control, and Dynamics*, vol. 32, no. 2, 2009.

[22] A. Durai, R. Dodamani, R. Antony, S. Chitlur, R. Gopalan, and S. Ahmed, "Experimental studies on a propelled micro air vehicle," in *29th AIAA Applied Aerodynamics Conference*, Honolulu, HI, 2011.

[23] Roskam, *Airplane Flight Dynamics and Automatic flight controls*, 1st ed. Darcorporation; Reprint edition, 2001.

[24] "Autonomous landing of a fixed-wing unmanned aerial vehcile using differential gps, by samuel jacobus adriaan smit," http://scholar.sun.ac.za/handle/10019.1/80122, accessed: 10/25/2015.

[25] "Sunsailor: Solar powered uav," http://www.hobbyking.com/hobbyking/store, accessed: 10/25/2015.

[26] D. Lundstrm, K. Amadori, and P. Krus, "Validation of models for small scale electric propulsion systems," in *48th AIAA Aerospace Sciences Meeting Including the New Horizons Forum and Aerospace Exposition*, Orlando, FL, 2010.

[27] J. Schoemann and M. Hornung, "Modeling of hybrid electric propulsion systems for small unmanned aerial vehicles," in *12th AIAA Aviation Technology, Integration, and Operations (ATIO) Conference and 14th AIAA/ISSMO Multidisciplinary Analysis and Optimization Conference*, Indianapolis, IN, 2012.

[28] R. Papdeja and P. Sankala, "Modelling and simulation of three phase brushless dc motor with using model reference adaptive controller," *International Journal of Inventions in Computer Science and Engineering*, vol. 1, no. 3, 2014.

[29] A. Kiruthika, A. Rajan, and P. Rajalakshmi, "Mathematical modelling and speed control of a sensored brushless dc motor using intelligent controller," in *Emerging Trends in Computing, Communication and Nanotechnology (ICE-CCN), 2013 International Conference on*, March 2013, pp. 211–216.

[30] "11x6 folding propeller," http://www.readymaderc.com/store/, accessed: 09/13/2015.

BIOGRAPHICAL STATEMENT

Sampath Reddy Vengate was born in Hyderabad, Telangana, India in 1992. He received his Bachelors in Aeronautical Engineering from Malla Reddy College of Engineering and Technology (a part of Jawaharlal Nehru Technological University). He is currently pursuing his Master's in Aerospace Engineering from The University of Texas Arlington and his research is on Development and Flight test of Moving-Mass Actuated Unmanned Aerial Vehicle.